PHYSICAL REVIEW B VOLUME 39, NUMBER 7 1 MARCH 1989

Two-dimensional angular correlation of annihilation radiation study of positron interactions with surfaces of aluminum

D. M. Chen*
City College of the City University of New York, Convent Avenue, New York, New York 10031

S. Berko and K. F. Canter
Brandeis University, Waltham, Massachusetts 02154

K. G. Lynn
Brookhaven National Laboratory, Upton, New York 11973

A. P. Mills Jr.
AT&T Bell Laboratories, Murray Hill, New Jersey, 07974

L. O. Roellig
City College of the City University of New York, Convent Avenue, New York, New York 10031

P. Sferlazzo
Brandeis University, Waltham, Massachusetts 02154

M. Weinert
Brookhaven National Laboratory, Upton, New York 11973

R. N. West
University of East Anglia, Norwich NR4 7TJ, England
(Received 6 July 1988)

Studies were made of the interactions of positrons with three low index surfaces of aluminum [(100), (110), and (111)] at room temperature with the aluminum surface at elevated temperatures and with oxygen adsorption on the aluminum surface. Our measurements using the improved two-dimensional angular correlation of annihilation radiation technique on surfaces support three established processes: spontaneous positronium (Ps) formation and emission, positrons bound in a surface state, and surface-state positrons thermally desorbed as Ps atoms. A method has been developed to accurately separate these components. The positron surface-state annihilation spectra are nearly isotropic for all three Al surfaces, which indicates a lateral localization and is inconsistent with either the ideal image-potential-induced bound state or the physisorbed Ps state. The thermal Ps momentum distributions agree well with the thermostatistical emission mechanism. The momentum distributions of the directly emitted Ps atoms are found to be very sensitive to the surface conditions, and to reflect the electron density of states near the surfaces, thus suggesting a new surface spectroscopy, angle-resolved Ps spectroscopy.

I. INTRODUCTION

Recently the technique of angular correlation of annihilation radiation (ACAR) has been applied to the study of positron interactions with surfaces.[1–6] This augmentation marks another important aspect of the growing field of positron surface physics.[7,8] Historically, the ACAR technique was established for bulk electronic structure and defect studies.[9,10] The feasibility of using this technique to study surface phenomena relies on confining the probing positrons to the near-surface region. Over the last few years there has been considerable progress in the construction of high-intensity, low-energy positron beams,[3] and it is now possible to produce a sufficient ACAR counting rate from well-characterized surfaces in order to obtain useful information. To date, measurement using this extended ACAR technique has been performed on surfaces of copper,[1] aluminum,[2–5] silicon,[5,6] nickel,[11] graphite,[12] and lead.[13] The results have shed new light on various positron-surface interaction mechanisms, and have raised some questions for further investigations.

When slow positrons impinge on a target surface, three major phenomena can occur:[7,8] Some of the thermalized positrons diffusing from the bulk to the surface are ejected into the vacuum if the positron work function is negative,[7] some take part in positronium (Ps) formation and emission, and some are captured into a surface state and can be liberated as Ps atoms by thermal activation. These surface-sensitive processes provide us complemen-

tary methods using the slow positrons as a probe to study crystallographic and electronic structures as well as other properties of surfaces. Like positron annihilation in a bulk material, the annihilation products from a positron trapped in the surface state or from a singlet-Ps atom formed near the surface are predominantly two γ photons ($\sim$511 keV). Thus the momentum distribution is uniquely contained in the annihilation pairs, and hence the interaction mechanisms involved can be well studied by the ACAR technique.

Following the first two surface ACAR measurements,[1-3] we have improved the ACAR resolution and statistics, and showed that the two-dimensional Ps momentum spectra for the three low index surfaces of Al exhibit anisotropic structures which were found to be very sensitive to the surface conditions and to reflect the electron density of states near the Fermi surface of Al.[4,5] Since Ps can only be formed near metal surfaces[14] with electrons from the occupied states within 2 to 3 eV from the Fermi level, these results have demonstrated a new surface spectroscopy: angle-resolved positronium emission spectroscopy, for the study of surface electronic structures. These advances confirmed the original suggestion of the Ps velocity spectroscopy made by Mills *et al.*[15] based on their time-of-flight (TOF) measurement of the Ps velocity distribution for an Al surface. In this paper we will elaborate and expand upon our previous report.[4]

Theoretically, the positron surface state has been treated either as an image-potential-induced bound state,[16-19] or as a physisorbed Ps state.[20] These two models have predicted a positron or a Ps wave function delocalized in the surface plane but localized perpendicular to the surface, which leads to a substantial anisotropic momentum distribution. As expected from the uncertainty principle, the confinement of the positron or Ps normal to the surface will result in a larger momentum component in that direction. However, the earlier two surface-state ACAR spectra measured for Cu and Al surfaces[1,2] as well as our more recent higher-precision data for three low index surfaces of Al have all yielded essentially isotropic distributions. This inconsistency with the theoretical models has led to the conjecture of the lateral localization of the positron wave function possibly due to the surface defects and impurities.[2,17(b)] Thus presently we are lacking a more realistic description of the positron surface state.

In the remainder of this paper we will provide a systematic discussion of our recent 2D ACAR study of positron interactions with three low index surfaces of aluminum. Because of its nearly free-electron-like band structure, bulk Al and Al surfaces have been investigated extensively, are well understood, and hence were chosen as a prototype for our study. In Sec. II we briefly describe our experimental setup and procedures. A qualitative discussion of several sets of directly measured spectra under various experimental conditions is given in Sec. III. After introducing in Sec. IV the data analysis technique which we developed, the positron-surface-state annihilation spectra and the Ps spectra are analyzed in considerable detail in Secs. V and VI, respectively. Theoretical predictions of the Ps spectra using projected Al band structures is also presented in Sec. VI. A thermally activated Ps spectrum is analyzed in Sec. VII. We summarize our discussion in Sec. VIII.

II. EXPERIMENTAL DETAILS

The present surface 2D ACAR measurement system consists of a high-intensity, slow positron beam, a pair of Anger cameras, and an ultra-high-vacuum (UHV) chamber equipped with typical surface tools as illustrated schematically in Fig. 1. The setup here differs from traditional 2D ACAR system in the following two aspects. (1) A conventional positron emitter with a β^+ spectrum (0–1 MeV) energy distribution is replaced by a high-intensity, energy tunable, monoenergetic beam of positrons. This is essential for controlling the positron implantation depth, and hence the fraction of the thermalized positrons

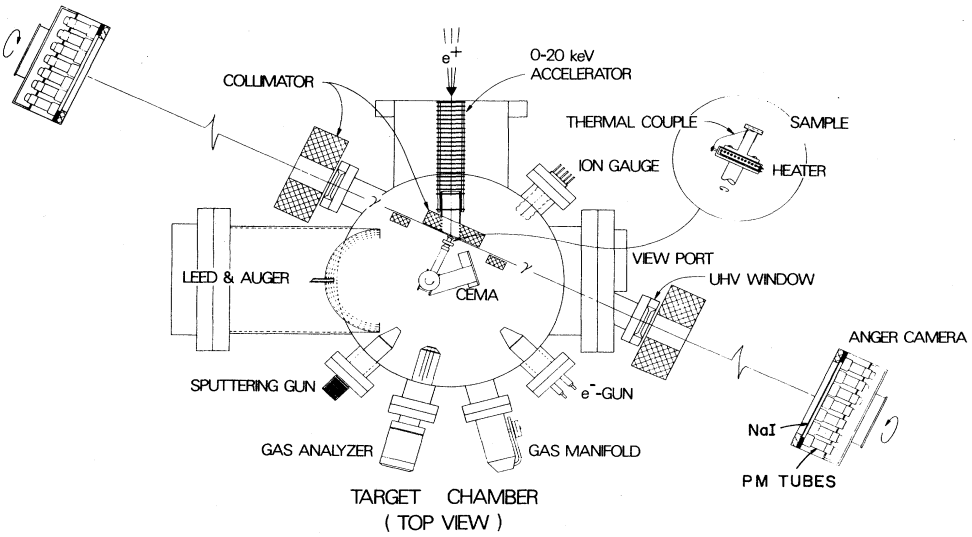

FIG. 1. Top view schematic of the target chamber and the Anger cameras (not to scale). The blowup shows the sample holder.

which can diffuse back to and interact with the surface under study. (2) The target chamber, the positron source chamber, and the beam line are joined together and form a UHV system necessary for both the surface studies and for the positron source preparation, energy moderation, and the beam transport.

Perhaps, the biggest challenge encountered in performing the surface ACAR experiment is to be able to accumulate data of high resolution and good statistics within a short time scale so that the sample surface condition will not alter appreciably during the whole measurement. This demands a good vacuum, a high e^+-beam intensity, and detectors of good spatial resolution and high detection efficiency. In the present work, using a beam of initial intensity of $\approx 7\times 10^7$ e^+/sec, an initial coincident rate of more than 15 cps was achieved with the Anger cameras located 11 m away from the sample which resulted in an overall resolution of 1 mrad FWHM by 1 mrad FWHM (1 mrad $\equiv mc\times 10^{-3}$ momentum units). Typically, an elapsed time of 3 h was necessary to yield 1000 counts at the peak channel.

A. The intense positron beam and the ACAR detector system

The high-intensity, slow positron beam was constructed at the high flux beam reactor (HFBR) of Brookhaven National Laboratory. Its design, performance, and future improvement have been discussed in detail elsewhere.[21] Briefly, a ^{64}Cu β^+ decay source is produced in the core of the HFBR by irradiating ^{63}Cu with a high flux of thermal neutrons ($8.3\times 10^{14} n_0$/cm^2 sec). A typical source of more than 20 Ci β^+ activity is obtained for a 100-mg pellet in 48-h irradiation. The ^{64}Cu source is then introduced through a load-lock chamber into a crucible in the source chamber where it is evaporated onto a single-crystal W(110) substrate, and subsequently annealed to form an epitaxy Cu(111) film of 1 cm^2 and 100-μm thick. This Cu film plays two important roles. It is an intense positron emitter as well as a positron energy moderator, which converts $\approx 0.01\%$ of the β^+ decay positrons into a monoenergetic positron source with a narrow energy width and small angular spread ($\sim 30°$). The emitted positrons are extracted away from the source by a set of $\mathbf{E}\times\mathbf{B}$ energy analyzers. An axial $\mathbf{B}$ field is generated to guide the beam. A linear accelerator was installed at the entrance of the surface chamber (Fig. 1) to obtain the desired incident positron energy and to direct the beam onto the target surface. At 200 eV the beam size is about 8 mm in diameter as displayed on a microchannel-electron-multiplier array.

Our two-dimensional, positron-sensitive detector system was a pair of Anger cameras and the associated electronics developed at the University of East Anglia. Table I lists the important performance specifications of these detectors. Detailed discussion about these detectors can be found in Ref. 22.

B. Sample preparation and characterization

All the samples used for the present investigations were cut into disks of 1-mm thick, 6.35-mm diam and were polished to a mirror finish. X-ray Laue pictures were taken for each sample to ensure a good single-crystal quality and an accuracy of selected crystalline orientations to less than 2°. As shown in the inset of Fig. 1, the sample was carefully mounted with hidden Ta wires on a Ta pedestal which was attached to the heater stage of a sample manipulator. A type-K thermal couple was affixed to the reverse side of the sample to monitor the sample temperature during annealing or high-temperature runs. The manipulator is also capable of azimuthal (ϕ) rotation, allowing the selection of the ACAR projection angle.

TABLE I. Anger camera specifications.

Single-camera detection area	0.11 m^2
Single-camera detection efficiency	$\sim 17\%$
Overall spatial resolution	10.86 mm
Background coincident rate	~ 0 cps
Data array dimensions	128×128
Camera-to-sample distance	11.14 m

The base pressure in the target chamber was 7×10^{-11} Torr, when the beam-line valve was closed. During measurements, however, the target chamber pressure rose to $2-3\times 10^{-10}$ Torr, due to the higher pressure in the beam line and source chamber. The Al sample was first outgassed and sputtered with $\sim 1-2$-kV Ar^+ at a glancing angle of incidence for 2–3 h. The ion current received by the sample was typically 10–15 μA/cm^2 in a constant flow of 1×10^{-4} Torr Ar gas. The damage of the sample surface resulting from ion bombardment was removed by annealing at ~ 620 K sample temperature. Prior to each run the sample was treated for one or more cycles of sputtering at lower energy (500–750 eV) and annealed for shorter time (30–60 min). The surface condition was monitored by low-energy electron diffraction (LEED) and Auger spectroscopy. For the present investigation the surface was considered to be clean when a correct LEED pattern of high quality (i.e., sharp and good contrast) was observed and impurity intensities detected by the Auger analyzer were below the noise level. In most of our work, we used a four-grid retarding-field Auger analyzer which has a noise-to-signal (main peak) ratio $N/S \approx \frac{1}{500}$. For later experiments a double-pass cylindrical analyzer was added into our system and hence a much better noise-to-signal ratio ($< \frac{1}{2000}$) was obtained. The Auger spectra taken with the double-pass cylindrical analyzer were also used to confirm the impurity levels estimated with the four-grid retarding-field Auger analyzer. For our cleaned surface the remaining impurities were estimated to be less than 0.03% of C *KLL* (~ 0.01 ML) and 1% of O *KLL* (~ 0.03 ML).

Due to reasons given in Sec. IV, each surface run was followed by a bulk run and our sample position could not be disturbed in between the two runs. Thus the surface could be examined only after the bulk run. The accumulation of impurities during the surface run was estimated by storing the data frequently during the measurement and by carefully comparing the separate runs afterwards. In addition, similar experimental conditions were simu-

lated when the positron beam was not in operation, and surface conditions were monitored after similar time durations. As is well known, difficulties arise from the recontamination of a cleaned surface, especially because of oxidation with the residual H_2O in the UHV system.[23] Our ACAR data showed a very high sensitivity to surface contamination. These findings will be incorporated in our data interpretations.

The monolayer oxygen on Al(100) was prepared by first preparing a clean surface before exposing it to 2×10^{-7} Torr 99.999% pure oxygen for 12 min. This led to a total exposure of ≈150 L (1 L$=1\times10^{-6}$ Torr sec), and corresponded to a coverage of ~1 ML.[23] After the exposure we observed a uniform fading of the original LEED pattern of the clean surface, and the Auger spectrum showed a reduction of the 68-eV peak associated with clean Al and an increase of the 51-eV peak indicating the presence of oxygen on Al surfaces. Several monolayers of oxide on Al(111) were produced by an exposure of $\approx3\times10^4$ L. The LEED pattern was completely extinguished after the exposure, and the O *KLL* Auger signal was detected. The thick-layer oxides were obtained from continuous O_2 exposure of the thin-layer oxide sample. The total exposure was increased to 1×10^6 L which lasted about another 60 h. In this case the Auger spectrum displayed no clean Al *LMM* signal, implying that the thickness of the oxide layer was ≥10 Å, the mean escaping depth of the 68-eV Auger electrons.

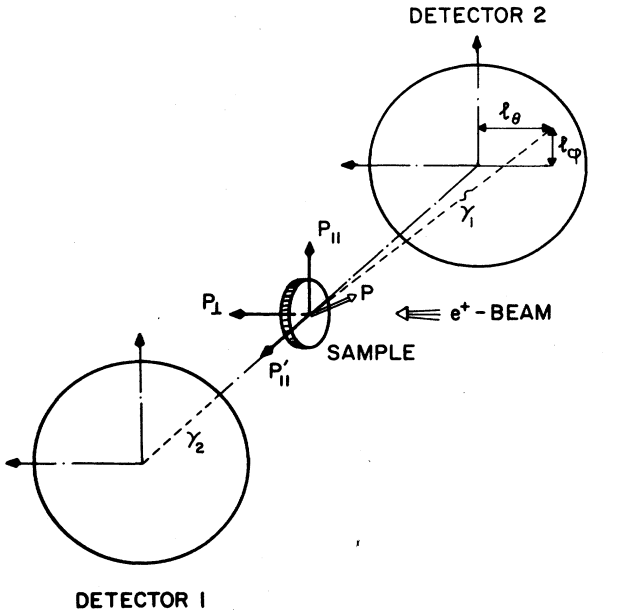

FIG. 2. The geometry of the 2D ACAR experiment: $\theta=p_\perp/m_ec$, $\phi=p_\parallel/m_ec$, and $p'_\parallel$ is integrated. The angle θ and ϕ are determined by the ratios of l_θ and l_ϕ to sample-to-detector distance.

III. EXPERIMENTAL RESULTS

The 2D ACAR experiment measures the 2D projection of the 3D momentum density of an initial state of the one-positron many-electron system or of the Ps atom formed at and emitted from the surface. For the geometry of the present experiment defined in Fig. 2, this can be expressed as

$$N(p_\perp,p_\parallel)=\int\rho(\mathbf{p})dp'_\parallel\ , \tag{1}$$

which, in practice, is convoluted with the detector resolution function. A surface 2D ACAR measurement in general contains surface state (SS) annihilation, annihilation of para-Ps formed at the surface, and a small fraction of bulk annihilation:

$$N_{\rm tot}(p_\perp,p_\parallel)=N_{\rm SS}(p_\perp,p_\parallel)+N_{\rm Ps}(p_\perp,p_\parallel)+N_{\rm bulk}(p_\perp,p_\parallel)\ . \tag{2}$$

A good example of various contributions is shown in Fig. 3, which is the perspective view of ACAR spectra measured for 3(a) an Al(111) surface at room temperature and 14.5-keV incident positron energy, 3(b) an Al(100) surface at room temperature and 1.5-keV incident energy, and 3(c) an Al(100) surface at 600 K and 1.5-keV incident energy. Figure 3(a) contains mainly the bulk annihilation, Fig. 3(b), the sum of the positron surface state and Ps annihilation, and Fig. 3(c), thermally activated and directly emitted positronium annihilation. To have a more complete view, ACAR spectra are often displayed as contour maps. The corresponding contours of Figs. 3(a)–3(c) are shown in Figs. 4(b), 6(a), and 6(b). We explain these spectra below.

Clearly, the usefulness of this technique relies very much on the possibility of separating the individual components. Nevertheless, a qualitative understanding of various positron-surface interaction processes can be made directly from the measured 2D ACAR spectra taken under different conditions.

A. Incident positron energy dependence

Figure 4 shows three contour plots of the room temperature 2D ACAR spectra for 4(a) an Al(111)-^{22}Na-Al(111) sandwich sample, 4(b) an Al(111) surface bombarded with 14.5-keV positrons, and 4(c) the same surface bombarded with 1.5-keV positrons. Their $p_\parallel=0$ sections are shown in Fig. 5. As is well known,[9] the bulk Al spectrum 5(a) is close to the projection of a Fermi sphere with a radius of ~6.8 mrad, reflecting the nearly free-electron-like conduction-band structure of Al. For $E=14.5$ keV, the spectrum 5(b) is mainly attributed to annihilation in the bulk, and hence is almost the same as the bulk spectrum 5(a), except that the central contours shift slightly towards the left due to a small fraction of Ps emission. Their agreement can also be observed in the 1D cuts [Fig. 5(a)]. When the incident positron energy is reduced to 1.5 keV [Fig. 4(c)] we observe an nonsymmetrical distribution indicating that majority of the incident positrons diffuse back to the surface and a fraction of them form Ps and escape into vacuum ($p_\perp<0$). The effect of Ps emission can be seen more clearly from the $p_\parallel=0$ sections in Fig. 5(a), and is responsible for the small

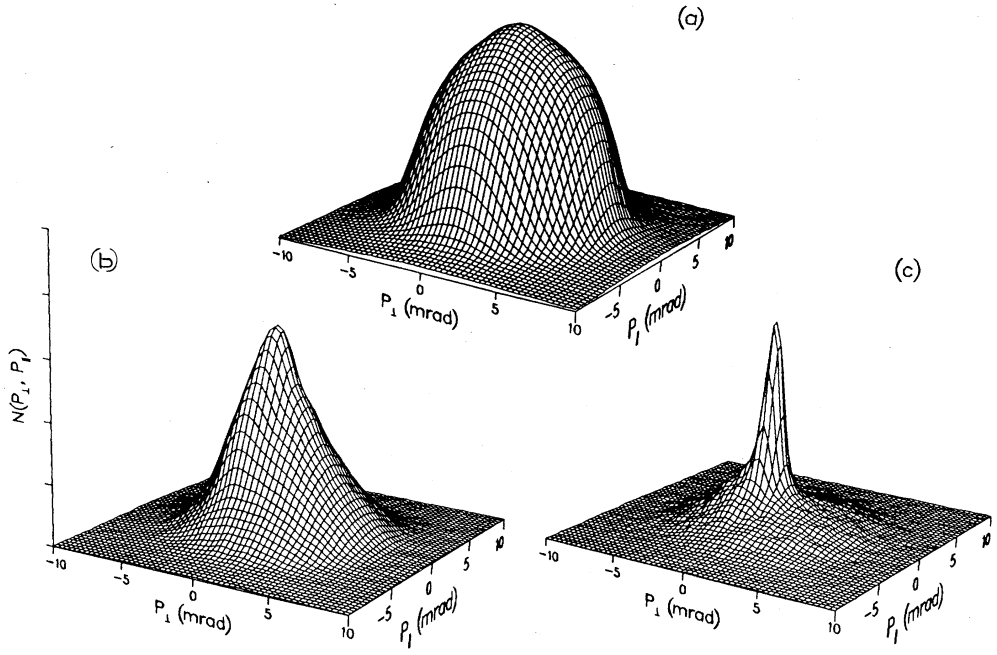

FIG. 3. Perspective representation of the peak-normalized 2D ACAR spectra for (a) an Al(111) surface at room temperature bombarded with 14.5-keV positrons, (b) an Al(100) surface at room temperature bombarded with 1.5-keV positrons, and (c) the same as (b) but the sample temperature is at 600 K.

plateau in the 1.5-keV curve. The $p_\perp > 0$ region contains a large percentage of the positron-surface-state annihilation, which is evidently much narrower than the bulk. The two small kinks at ± 5.5 mrad are the result of some residual bulk annihilation. Similar changes associated with the different incident positron energies have also been observed for Al(100) and Al(110) surfaces.

B. Temperature effect

Figure 6 compares the measured ACAR spectra from an Al(100) sample at room temperature [6(a)], at 600 K [6(b)], and at 750 K [6(c)]. The positron beam energy is 1.5 keV for 6(a) and 6(b), and 5 keV for 6(c). In order to see the intense peak structure graph 6(b) is plotted with 9 contours instead of 14 as there are in 6(a) and 6(c). Figure 5(b) corresponds to their $p_\parallel = 0$ sections. The perspective representations of 6(a) and 6(b) are shown in Figs. 3(b) and 3(c). The substantial change of the 2D ACAR spectrum from room temperature to 600 K then to 750 K clearly marks the occurrence of different interaction processes. At 600 K, the emergence of the sharp narrow peak around $p_\perp = -0.5$ mrad with a large reduction of the contribution in the region of $p_\perp > 0$, shows that positrons trapped in surface states at room temperature were liberated from the surface as thermal

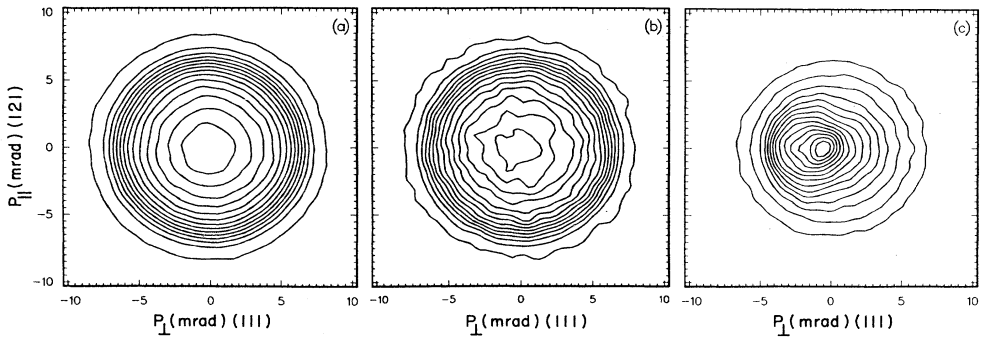

FIG. 4. 2D contour plots of the directly measured ACAR spectrum for (a) an Al(111)-^{22}Na-Al(111) bulk sample; (b) an Al(111) surface bombarded with a 14.5-keV positron beam; and (c) the same surface bombarded with a 1.5-keV positron beam. Each spectrum contains the same number of contours with a constant step. The crystal index along each axis is also labeled.

Ps atoms.[24] Note that this temperature (600 K) was chosen in accordance with the previous study[8] to obtain a maximum thermal Ps desorption yield. Beyond this temperature bulk vacancies begin to be activated. Thus at 750 K and 5-keV incident energy, a large fraction of the incident positrons are effectively captured in the vacancies, the total Ps fraction drops dramatically, and the overall annihilation spectrum is much broader.[25]

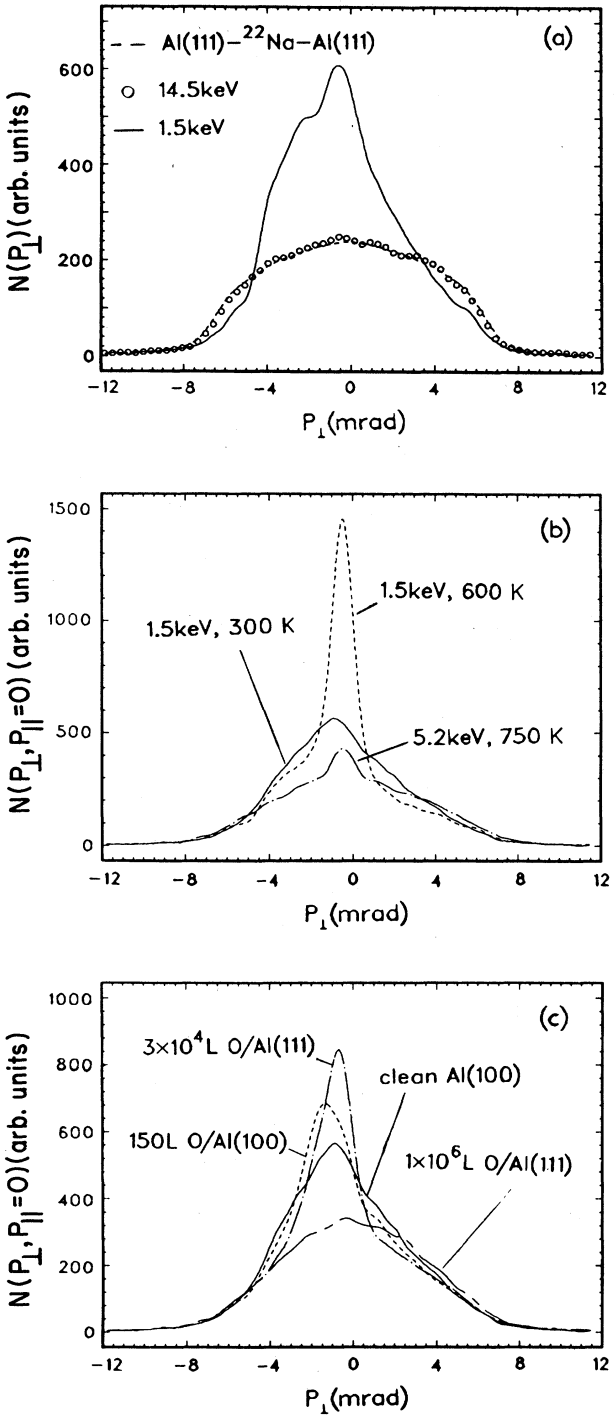

FIG. 5. (a) $p_\parallel=0$ sections of Fig. 4; (b) $p_\parallel=0$ sections of Fig. 6; and (c) $p_\parallel=0$ sections of Figs. 6(a) and 7. For each frame the cuts are taken from the volume-normalized 2D spectra.

C. Oxygen coverage

The ACAR results for three oxygen coverage on Al surfaces with the same incident positron energy of 1.5 keV are shown in Fig. 7: 7(a) 150 L on Al(100); 7(b) 3×10^4 L on Al(111); and 7(c) 1×10^6 L on Al(111). Their sections at $p_\parallel=0$ are shown in Fig. 5(c). For comparison the curve for a clean Al(100) spectrum [Fig. 6(a)] is also plotted. Comparing the contour plots we see that some structure that appears in Fig. 6(a) has been smeared out when the Al(100) surface is exposed to 150 L oxygen [Fig. 7(a)]. The latter also results in a narrowing in the Ps distribution and in a small increase in total Ps emission fraction. Since this exposure leads to only a monolayer oxygen coverage, the structure associated with the clean Al(100) sample must be a surface effect. Figure 7(b) shows that the Ps contribution is even sharper and narrower at higher oxygen exposure. In this case a layer of Al oxide is grown on the Al(111) surface the Ps spectrum mainly reflects the electronic property of the oxide rather than the metal substrate. When the exposure is increased to 1×10^6 L, the spectrum [Fig. 7(c)] changed completely. Ps emission is almost suppressed. This is a clear indication of positrons being trapped in the disordered oxide layers or possibly in the interface region due to the increased thickness of the Al oxide layer (~10 Å). These results are all in good agreement with the earlier Ps fraction measurements.[8]

D. Crystal orientation dependence

Figure 8 represents the ACAR spectra taken at 1.5-keV incident energy for Al(111), Al(100), and Al(110) surfaces. All three spectra are symmetrized with respect to the $p_\perp$ axis (i.e., a σ plane) to improve the statistics. This improvement is apparent when one compares 8(a) and 8(b) with their original versions in Fig. 4(c) and Fig. 6(a). It is clear that the right halves ($p_\perp>0$) of 8(a)–8(c) are similar to each other. On the left side ($p_\perp<0$), the Al(111) spectrum 8(a) is closer to the Al(110) 8(c) but the two are very different from the Al(100) spectrum 8(b). The (100) spectrum displays two side lobes that are absent in both the (111) and the (110) spectra. This suggests that the Ps momentum distribution depends much more strongly on the crystal orientations than the positron-surface-state annihilation. It will be shown that these structural differences can be attributed to the differences among the projected electronic band structures, and to a lesser extent, to the different amount of surface contamination. We have also inspected the azimuthal dependence of the surface ACAR spectrum for both the Al(100) and Al(110) surfaces. With our present detector resolution the results are essentially indistinguishable.

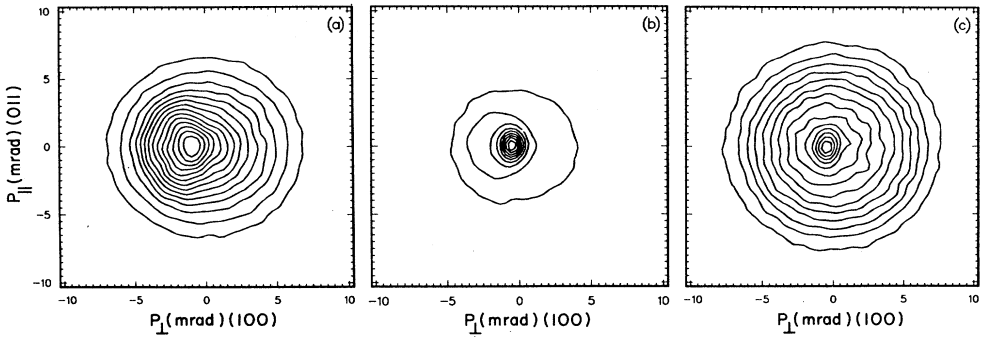

FIG. 6. Contour plots of the Al(100) surface ACAR spectra. The positron beam energy and sample temperature are (a) 1.5 keV, 300 K; (b) 1.5 keV, 600 K; and (c) 5.0 keV, 750 K. For clarity, (b) is plotted with 9 contours while (a) and (c) have 14 contours each.

IV. DATA SEPARATION

A more precise understanding of the above ACAR spectra requires a separate analysis of the various contributions. Fortunately, by using the underlying symmetries of these contributions, and the well-studied positron implantation and diffusion process in bulk material, the measured spectra can be decomposed into three components.[5] From time-reversal symmetry it can be shown that the momentum density functions of the positron-surface-state annihilation and bulk annihilation possess inversion symmetry with respect to the momentum $\mathbf{p}$. This symmetry is preserved in the 2D ACAR projection since the detector's nonlinearity is sufficiently small, and hence the resolution function is isotropic. Therefore,

$$N_{SS}(p_{\perp},p_{\parallel})=N_{SS}(-p_{\perp},-p_{\parallel}) , \tag{3}$$

$$N_{bulk}(p_{\perp},p_{\parallel})=N_{bulk}(-p_{\perp},-p_{\parallel}) . \tag{4}$$

Although Ps atoms can only be emitted into the vacuum, i.e., the Ps momentum density $\rho_{Ps}(\mathbf{p})=0$ for $p_{\perp}\geq 0$ (see Fig. 2), the smearing introduced by the finite detector resolution leads to

$$N_{Ps}(p_{\perp},p_{\parallel})\neq 0 \quad \text{for } 0\leq p_{\perp}\leq \epsilon , \tag{5}$$

where ϵ is on the order of the FWHM (full-width at half maximum) of the overall detector resolution function. In an ideal situation the resolution function becomes a δ-function and $\epsilon\rightarrow 0$. In this limit,

$$N_{tot}(p_{\perp},p_{\parallel})=\begin{cases} N_{SS}(p_{\perp},p_{\parallel})+N_{bulk}(p_{\perp},p_{\parallel})+N_{Ps}(p_{\perp},p_{\parallel}), & p_{\perp}\leq 0 , \\ N_{SS}(p_{\perp},p_{\parallel})+N_{bulk}(p_{\perp},p_{\parallel}), & p_{\perp}>0 , \end{cases} \tag{6}$$

thus

$$N_{Ps}(p_{\perp},p_{\parallel})=\begin{cases} N_{tot}(p_{\perp},p_{\parallel})-N_{tot}(-p_{\perp},p_{\parallel}), & p_{\perp}\leq 0 , \\ 0, & p_{\perp}>0 . \end{cases} \tag{7}$$

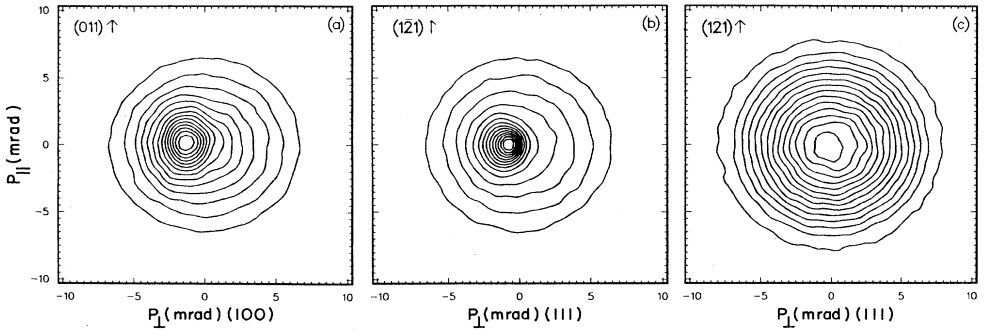

FIG. 7. Contour plots of the ACAR spectra for oxygen-covered Al surface. (a) 150 L/Al(100); (b) 3×10^4 L/Al(111); and (c) 1×10^6 L/Al(111). The beam energy is 1.5 keV for all runs.

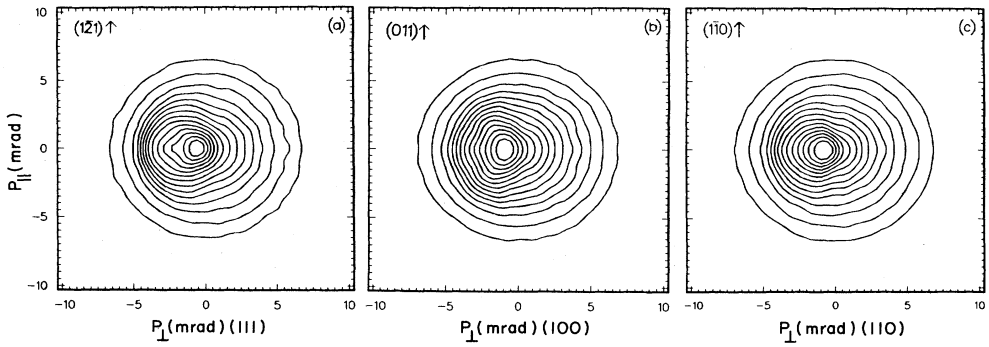

FIG. 8. (a)–(c) Contour plots of the symmetrized ACAR spectra for clean surfaces of Al(111), Al(100), and Al(110). All three spectra were taken at room temperature and 1.5-keV incident energy. The unsymmetrized versions of (a) and (b) are Figs. 4(c) and 6(a).

The Ps component of a measured 2D ACAR spectrum is therefore extracted from a simple "inversion subtraction," a name by which we will refer to the operation of Eq. (7) henceforth.

However, for finite detector resolution $\epsilon \neq 0$, the direct inversion subtraction of the measured spectra leads to some inevitable distortions to the true spectra in the region $-\epsilon \leq p_\perp \leq \epsilon$. It leaves some extra counts in $N_{SS}(p_\perp, p_\parallel)$ and over subtracts $N_{Ps}(p_\perp, p_\parallel)$. In principle, the distortion can be recovered by employing a deconvolution technique prior to the inversion subtraction. Therefore we can separate the directly measured spectrum into a Ps component and a symmetrical component (of inversion symmetry). The price one pays here is that the information carried in the symmetrical part of the spectrum can be extracted from only half of the measured spectrum ($p_\perp \geq 0$), and the other half provides the Ps spectrum.[26]

The symmetrical part of the spectrum is the sum of the surface-state annihilation and the bulk annihilation. The relative contributions of these two components are determined by the controlled-incident beam energy. At low-incident energy (< 100 eV) the bulk annihilation is negligible, while at high energy (15 keV) the annihilations occur mostly in the bulk. It may appear that separation of the bulk component can be avoided if one uses a sufficiently low-incident energy for the measurement. Unfortunately, at low-incident energy (< 100 eV) the fraction of incident positrons returning to the surface before they are thermalized can be significant, and this can complicate the interpretation of our measurement. Therefore in all our surface measurements for Al, we have selected $E = 1.5$ keV, for which the bulk contribution cannot be ignored. Nevertheless, using the diffusion equation[7,8] one can determine the relative bulk fraction, and N_{SS} can be obtained by subtracting a properly normalized high-energy spectrum from a low-energy spectrum.

In our analysis, the deconvolution is done by the van Cittert's iteration algorithm[5,27] with a Gaussian resolution function. After the separation, the decomposed spectra are convoluted back so that the final results only weakly depend on the details of the resolution function used. The most critical point of our analysis scheme is the determination of the position of $p_\perp = 0$ with respect to a measured spectrum. We have taken advantage of the reflection symmetry of the "long-slit"[28] bulk spectrum to deduce the symmetrical center. Each low-energy run was followed by a high-energy run without altering the sample position in between. The center deduced from the high-energy run, which contains essentially the bulk annihilation, is assigned to be the center of the surface run. In fact, most of the long-slit surface spectrum $N(p_\parallel)$ also possesses reflection symmetry with respect to $p_\parallel = 0$. We have verified that the accuracy of this method is within 0.04 mrad, but the drawback of it is the lack of immediate examination of the surface condition after the measurement.

Most of the low index surfaces still maintain a reflection symmetry with respect to the $p_\perp$ axis, and therefore allow us to symmetrize the ACAR spectrum to improve the statistics. Rigorously speaking, the symmetrization is legitimate only if (i) the detectors have perfect linearity and uniformity, (ii) the crystal axis is perfectly aligned with the detectors axis, (iii) the center position of the spectrum is known exactly, and (iv) the crystal surface maintains the same symmetry as the bulk termination. In reality, these conditions can only be optimized, and the symmetrized results should be inspected with great caution, especially for data of low statistics. We have performed some simulation test to ensure that the symmetrization and separation of our data are justifiable.

Our analysis procedures are discussed in more detail in the Appendix. To illustrate this method, Fig. 9 shows the original and the decomposed spectra in their one-dimensional cuts at $p_\parallel = 0$ for an Al(100) surface using a 1.5 keV positron beam. In Fig. 9(a) the triangles represent the total measurement, circles are the generated symmetrical distribution and diamonds are the differences between the total and the symmetrical distributions, i.e., the separated Ps spectrum. The identity between the total and the symmetrical in the region $p_\perp > 0.5$ and $p_\perp < -6$ mrad reflects the reliability of our data-separation technique and the accuracy of our zero $p_\perp$ determination. The deconvolution step assures that the symmetrical curve turns over to the left in a natural way, as expected from the finite-detector resolution, to avoid

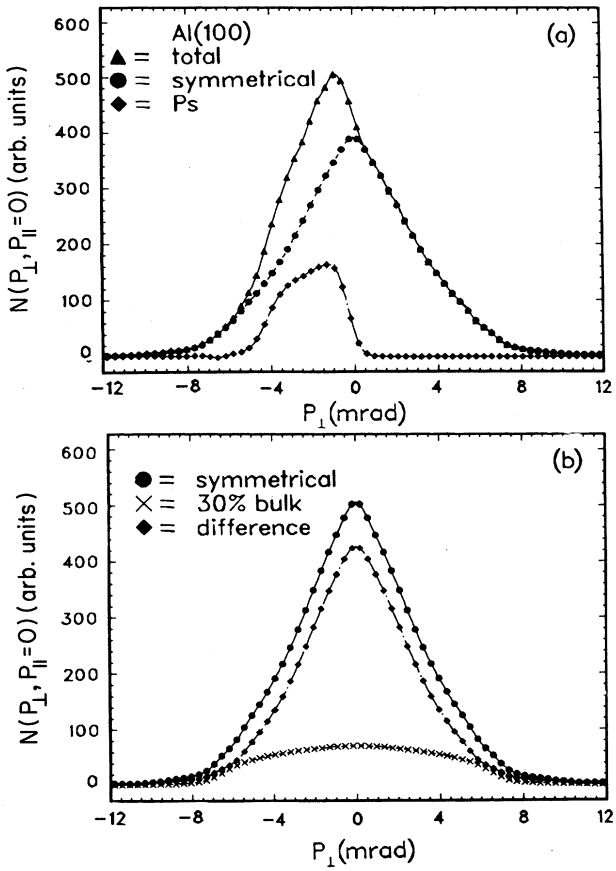

FIG. 9. Illustration of the data separation. (a) $p_{\parallel}=0$ sections of the directly measured ACAR spectrum (triangles), the separated symmetrical part (circles), and the separated Ps spectrum (diamonds) for an Al(100) surface. The incident positron energy is 1.5 keV; (b) $p_{\parallel}=0$ sections of the above symmetrical spectrum (now in circles), a 30 vol % bulk-Al spectrum (crosses) and their difference (diamonds), i.e., the surface-state spectrum.

the unphysical sharpness that would occur otherwise at $p_{\perp}=0$. The Ps distribution terminates at ~ -5 mrad. This is expected since the -2.6-eV Ps work function for Al[15] converts to a maximum-allowed Ps momentum of $q_M=4.5$ mrad and our apparatus resolution is about 1 mrad FWHM. The separated symmetrical spectrum still contains some fraction of the bulk annihilation. For an incident energy of 1.5 keV, it is estimated from Eqs. (A6)–(A8) that the symmetrical spectrum contains 30 vol % bulk contribution. Figure 9(b) shows the symmetrical spectrum in circles, the 30 vol % bulk in crosses, and the difference, the surface state in diamonds.

V. POSITRON SURFACE-STATE ANNIHILATION

A. The ACAR results

Figure 10 shows a set of separated surface-state spectra for Al(111), Al(100), and Al(110) surfaces. They are obtained from the original spectra shown in Fig. 8. The three spectra are similar, and exhibit only a small elongated shape in the outer contours, the $p_{\perp}$ direction being slightly longer than the $p_{\parallel}$ direction. To examine the anisotropy between the normal and parallel distributions, the long-slit projection[28] along these two directions are generated and plotted in Fig. 11 after the peak normalization. In all three sets of curves, the parallel distributions are only slightly narrower than the normal distributions. The shapes of the three sets of curves are essentially the same, and the FWHM is 6.3 mrad. When comparing the sections of $p_{\parallel}=0$ with those of $p_{\perp}=0$, we observed a similar but smaller difference between the two orthogonal directions. It should be mentioned that the uncertainty in the position of $p_{\perp}=0$ and $p_{\parallel}=0$ and in the detector resolution function will affect the widths of these surface-state spectra, and therefore should be inspected carefully. In Figs. 10 and 11, a small distortion from the true surface-state spectra in the vicinity of $p_{\perp}=0$ may still be retained, especially for the Al(111) spectrum. However, the smearing of Ps distribution into $p_{\perp}>0$ region due to the finite detector resolution can extend no more than ~ 1.5 mrad (3σ). Beyond that the directly measured spectrum is purely from the surface-state annihilation. Thus we have also compared cuts made at $p_{\parallel}=1.7$ and $p_{\perp}=1.7$ mrad from the originally measured spectra. The results are consistent with the conclusion drawn from the contour and long-slit spectra. Furthermore, taking into account the sample size effect will only

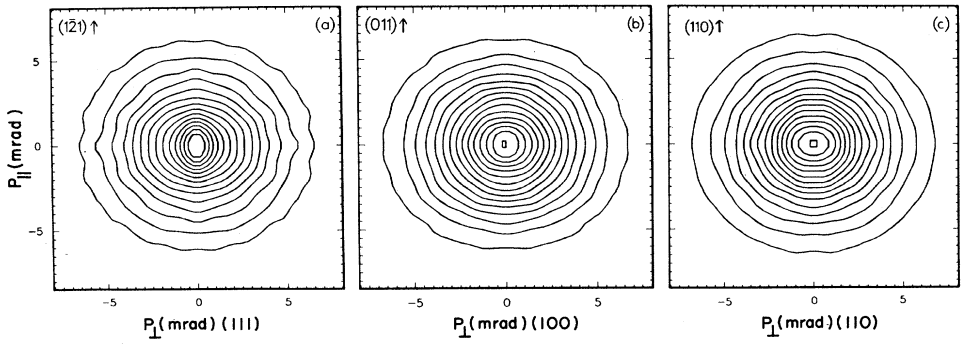

FIG. 10. (a)–(c) The separated positron surface-state spectra for Al(111), Al(100), and Al(110) surfaces. They are extracted from Figs. 8(a)–8(c).

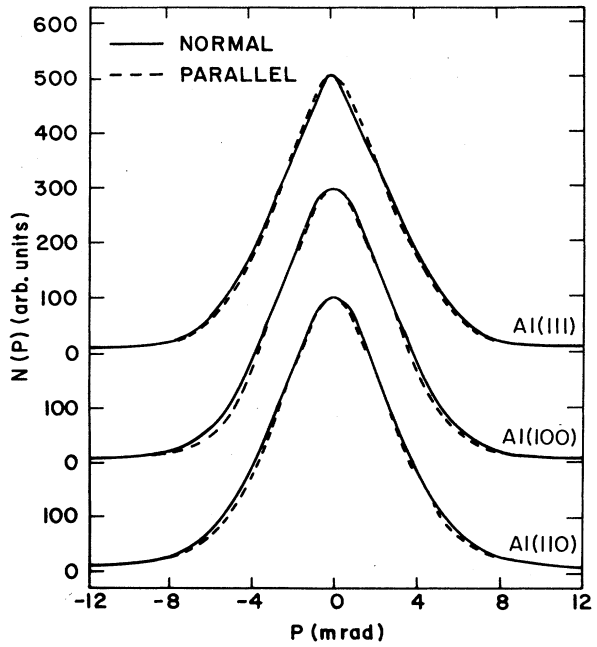

FIG. 11. Normal and parallel long-slit spectra generated from the three surface-state spectra shown in Fig.10.

result in narrowing the parallel distribution slightly. It is appropriate to conclude that for three low index surfaces of Al, the positron surface-state annihilation spectrum is nearly isotropic.

B. Discussion

Our ACAR measurement with improved detector resolution and statistics has also been carried out for silicon and nickel surfaces. All these results support the earlier conclusion of Lynn *et al.*[2] that no substantial anisotropy has been found in the positron surface-state ACAR spectra. Thus it is inconsistent with either the image-potential-induced surface state or the physisorbed Ps state. Using the static image potential ($V \sim -1/z$), Nieminen and Manninen[16(b)] have predicted a large anisotropy between the long-slit ACAR spectra[28] parallel and perpendicular to the surface. When the spectra are area normalized the peak height of the parallel distribution is twice that of the normal, indicating a substantial broadening in the normal momentum component due to the positron localization perpendicular to the surface. It was found that the large anisotropy was independent of the model potentials, some of which includes the dynamical nature of the image interaction, and the effective image plane in the classical static potential [$V \sim -1/(z-z_0)$] to account for the e^+-e^- correlation near the surface. Brown, Walker, and West[17(a)] recently have shown that using the Lang-Kohn electron density, the mixed density approximation (MDA) yields lesser anisotropy than the independent particle model (IPM), and the MDA calculation for the classical static potential ($-1/z$) results in a much smaller anisotropy than the screened potential [$1/(z-z_0)$]. Figure 12 shows a comparison of their optimized theoretical contour for an Al surface with our experimental spectrum for an Al(100) surface.

In contrast to the bulk-Al spectrum [Figs. 4(a) and 5(a)], the surface-state spectra (Figs. 10 and 11) exhibit a narrow conical shape, reflecting the inhomogeneous electron density at the surface. Despite the substantial anisotropy, the image-potential-induced positron surface state does give rise to a distribution of similar shape with comparable widths.[16-19] Because of the presence of the surface barrier, electrons with larger perpendicular crystal momentum $k_\perp$ can be extended further away from the surface and have a higher probability annihilating with

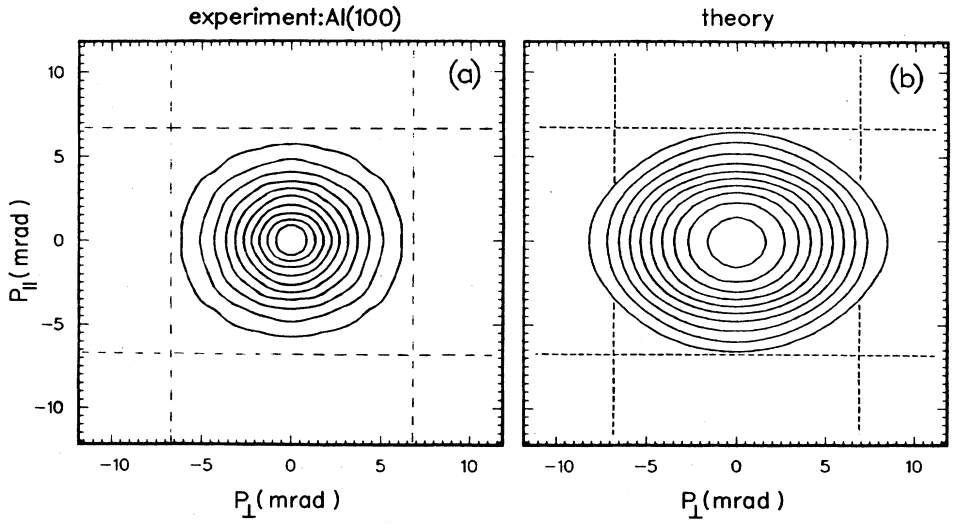

FIG. 12. Positron surface state ACAR spectra. (a) An experimental spectrum for an Al(100) surface and (b) the optimize theoretical prediction of Brown, Walker, and West (Ref. 17).

the positron trapped in the image potential well. Thus on one hand, the spherical Fermi surface of Al requires these electrons to have small $k_{\parallel}$ and hence leads to a narrow annihilation spectrum parallel to the surface. On the other hand, in the barrier region the electron potential rises and hence the momentum perpendicular to the surface decreases accordingly, which results in a narrower contribution to the normal distribution. The total normal width depends also on the positron binding potential. In another jellium-model calculation[18] Garner and Benedek showed that using a ~ 1-Å-wide square potential well for the positron state, the averaged positron momentum contributes to half of the total width in the normal distribution. Lou *et al.*[19] claim that with some proper adjustment of parameters, their calculation yields an isotropic positron surface-state ACAR spectrum.

In the physisorbed Ps picture of Platzman and Tzoar[20] the 2γ angular correlation distribution reflects the center-of-mass (c.m.) motion of the weakly bound $(-1/z^3)$ Ps atom. Normal to the surface, they found approximately a Lorentzian squared long-slit distribution with a full width of 4.8 mrad. To avoid the large anisotropy as would be required by the uncertainty principle, they argued that the parallel angular correlation can arise from the recoil momentum of the c.m. due to the emission and reabsorption of surface plasmons via a higher-order virtual process, which leads to the total spectrum being isotropic. However the calculated 4.8-mrad full width is about 20% narrower than our experimental results. We recall that in low-density insulator crystals (e.g., quartz, ice), Ps atoms formed in the bulk material annihilate in a large fraction via a pick-off process,[29] in which the positron of an ortho-Ps annihilates with a host electron of opposite spin to the one on the Ps. The pick-off process produces a very broad momentum distribution. Similar process may also need to be considered in the physisorbed Ps model.

The lack of a substantial anisotropy in our measured positron surface-state spectra may suggest that the positron surface state is not extended in the surface plane. It is pointed out in Ref. 2 that the planar localization of the surface state could be induced by some surface defects, or by surface impurities. However, comparing a series of time sequential measurements we found that the surface-state ACAR spectra are insensitive to oxygen contamination from 2% to 10% of a monolayer. From a more realistic discrete-lattice calculation[16(c)] for the image-induced positron surface state, Nieminen and Puska found that for a corrugated-image plane, no vacancy-trapped states exist on Al surfaces, while for a fixed effective image plane, a stable surface vacancy state exists on Al(110), but not on Al(100) and Al(111). Brown, Jensen, and Walker[17(b)] have extended the similar computation to investigate the possibility of trapping at ledges and multivacancies. Again, they concluded that for the corrugated image plane, localized states at vacancies and ledges are unstable with respect to the delocalized state for these three Al surfaces. However, trapping at multivacancies on all three surfaces are energetically favorable when the fixed-image plane was used. Although the theoretical predictions of a surface localized state has strong model dependence, the calculations of Brown, Jensen, and Walker show that the ACAR spectrum for a positron localized in a surface monovacancy is nearly isotropic and hence is in good agreement with our experimental observations. Nieminen and Puska have also predicted that the positron diffusion constant $D_+ = 1.4$ cm^2/sec on Al surfaces. This, together with the measured surface-state lifetime of 580 psec for the Al(110) surface,[30] corresponds to a lateral diffusion length of ~ 3000 Å. If the positron was to be trapped in some surface defect, the lack of anisotropy then might imply that the upper limit of the surface defect concentration is $\sim 1/(3000\ \text{Å})^2$.

To date no theoretical computations for the 2γ angular correlation spectrum have been performed using a realistic electronic band structure. As will be shown in the next section the surface-projected band structures of three low index surfaces of Al are very different. Substantial band gaps appear near the Fermi level for the (100) and the (110) face. However, our measurement show very little variations among the positron surface-state ACAR spectra for these surfaces. In addition, the fact that small contamination (0.01–0.1 ML) of oxygen does not change the ACAR spectrum noticeably is also somewhat surprising, since the theoretical calculation[31] showed that the O_2 p electrons are highly surface localized and form bands of ~ 3-eV width lying approximately 6.5 eV below the Fermi level. Theoretical investigations including these aspects should help us understand the nature of the positron surface state.

VI. POSITRONIUM EMISSION SPECTROSCOPY

A. ACAR spectra of the emitted positronium

Figures 13 and 14 show two sets of separated Ps spectra, each containing $\sim 4\times 10^4$ counts. The spectra are obtained from the symmetrized versions of the original measurements using a 1.5-keV positron beam. Note that the contours are rotated 90° clockwise from the previous presentations. The crystal orientations along the two resolved momentum directions are indicated in the lower left corner and the total-Ps fractions are given in upper left. These total-Ps fractions deduced from Eqs. (A4)–(A6) have less than $\pm 3\%$ error and are in good agreement with previous Ps fraction measurements.[7,8] Figures 13(a)–13(c) are for clean Al(111), Al(100), and Al(110) surfaces, respectively. All the runs started with less than 0.01 ML carbon and 0.01 ML oxygen impurities. At the end of the measurements the carbon level remained the same and the oxygen increased to ~ 0.05 ML for the Al(111) and Al(100) surfaces, but to ~ 0.1 ML for the Al(110) runs since this face has highest-oxygen-sticking coefficient.[23] Unlike the surface-state spectra (Fig. 10), the Ps spectra strongly depend on the crystal orientations. While both Al(111) and Al(110) spectra [10(a) and 10(c)] display a nearly isotropic shape, the Al(100) spectrum 10(b) shows a clear anisotropy characterized by the three statistically significant lobes. In fact, these structural differences are hinted in the directly measured spectra shown in Fig. 8. The common

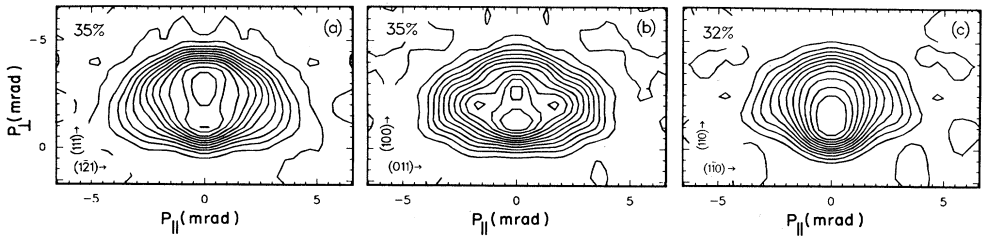

FIG. 13. (a)–(c) Experimental Ps spectra for Al(111), Al(100), and Al(110) surfaces. They are obtained from the spectra in Fig. 8, but are rotated 90° clockwise. The total Ps fraction deduced for each measurement is given in the upper left corner.

features appear in all three Ps spectra are the semicircular cutoff at the maximum-allowed positronium momentum for Al, $q_M = 4.5$ mrad, and the sharp rise near the origin, especially for the Al(110) spectrum. Figure 14(a) is for the same clean Al(100) surface as Fig. 13(b), but with a 45° azimuthal rotations; 14(b) is for an Al(100) surface exposed to 150 L oxygen corresponding to 1 ML coverage; 14(c) is for the Al(111) surface [Fig. 13(a)] exposed to 3×10^4 L oxygen. The 45° azimuthal rotation [Fig. 14(a)] of the projection angle does not change the Ps spectrum for the Al(100) surface [Fig. 13(b)] appreciably. Likewise, a 90° azimuthal rotation of the Al(110) surface yielded essentially the same spectrum as Fig. 13(c). However, the three lobes present in the clean Al(100) spectra [Figs. 13(b) and 14(a)] disappear when the surface is exposed to 150 L oxygen [Fig. 14(b)]. The 1-ML oxygen coverage on the Al(100) surface also results in a smaller distribution and higher Ps fraction. The thin-oxide layer on the Al(111) surface produces a much narrower Ps spectrum [Fig. 14(c)] with a most probable momentum of ~ 1 mrad (i.e., a most probable energy of ~ 130 meV).

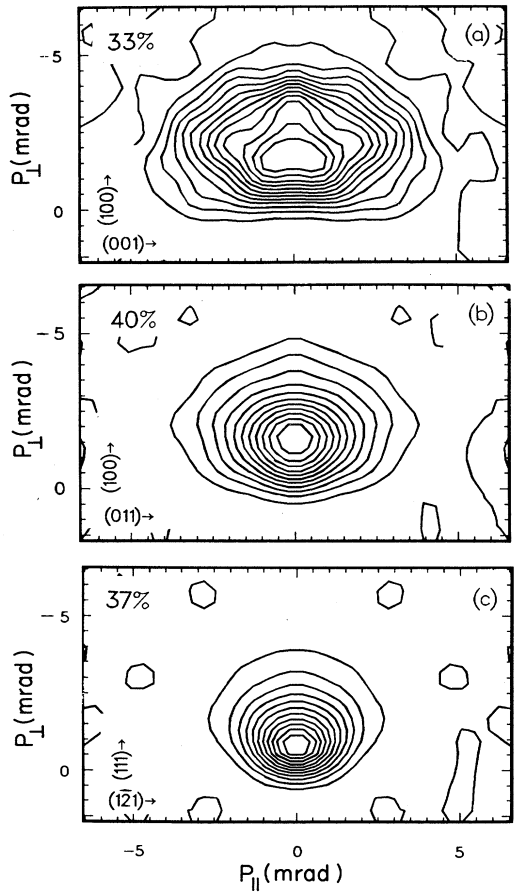

FIG. 14. Separated Ps spectra for (a) the same Al(100) surface as Fig. 13(b) subject to a 45° azimuthal rotation; (b) the same as (a) but with a 150 L oxygen exposure; and (c) the same Al(111) surface as Fig. 13(a) with 3×10^4 L oxygen exposure.

The three lobes in the clean Al(100) Ps spectra were reproduced from several Al(100) surfaces, but never appear in the spectra of the other two faces of Al, or of the surfaces of Si and Ni. An inspection of the unsymmetrized version of the Al(100) Ps spectra also proves that these lobes are indeed statistically significant. The fact that the anisotropy of the Ps spectra for Al(100) is very sensitive to the oxygen impurity in the surface, suggests that the anisotropy is associated with the clean Al(100) surface only. To study this effect in further detail we have performed a sequential run with 3 h each, following the initial preparation of the Al(100) sample. The results are shown in Fig. 15, where each spectrum [15(a)–15(d)] contains a total of $\sim 1\times10^4$ counts. We note that the anisotropy present in the first run 15(a) gradually diminishes and the momentum distribution narrows as we move towards the last run 15(d). The detail of this trend can be seen more clearly from the normal ($p_\parallel = 0$) and parallel ($p_\perp = -1.5$ mrad) sections shown in Fig. 16. The narrower component peaked at $\sim p_\perp = -1.5$ mrad increases as we progress from 16(a)–16(d). After the first run the contamination was roughly the same as it was initially, ≈ 0.006 ML C and ≈ 0.01 ML O as determined by a double-pass cylindrical mirror Auger analyzer. After the fourth run [frame 15(d)] the C level was unchanged, but the O was found to have increased to 0.12 ML. Thus we can attribute the above effect to an increasing oxygen contamination, and the anisotropy to the clean Al(100) surface.

B. Momentum density of the Ps emission

The Ps work function is defined as the sum of the electron and positron work function minus $\frac{1}{2}R_y$, the Ps vacu-

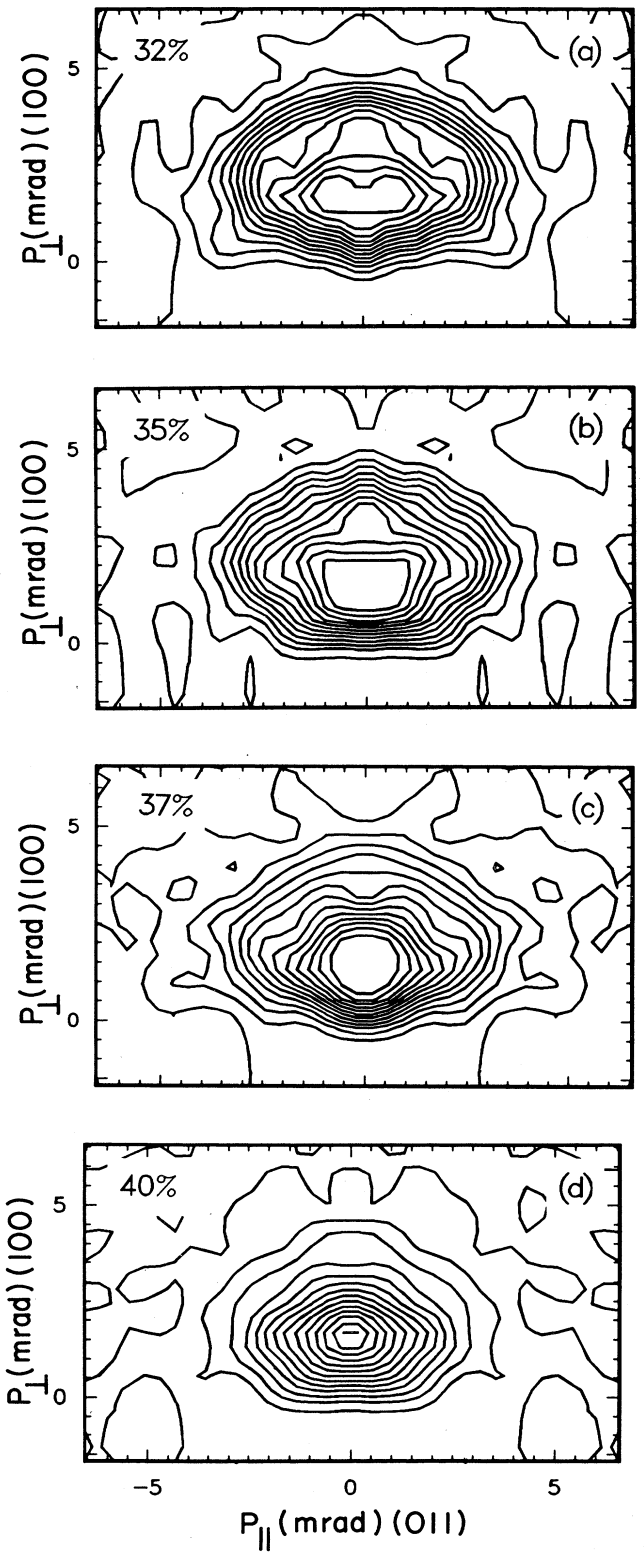

FIG. 15. Ps spectra of four sequential measurements for an Al(100) surface, time duration for each spectrum is 3 h, the observed change is due to the increasing oxygen contamination from the initial level of 0.01% of a monolayer to 0.10% of a monolayer at the end of the measurement.

um binding energy:

$$\Phi_{Ps}=\Phi_{-}+\Phi_{+}-6.8\ \text{eV}\ . \tag{8}$$

For many metal and semiconductor surfaces, Φ_{-} is about 4 eV, and Φ_{+} is either negative or only slightly positive,

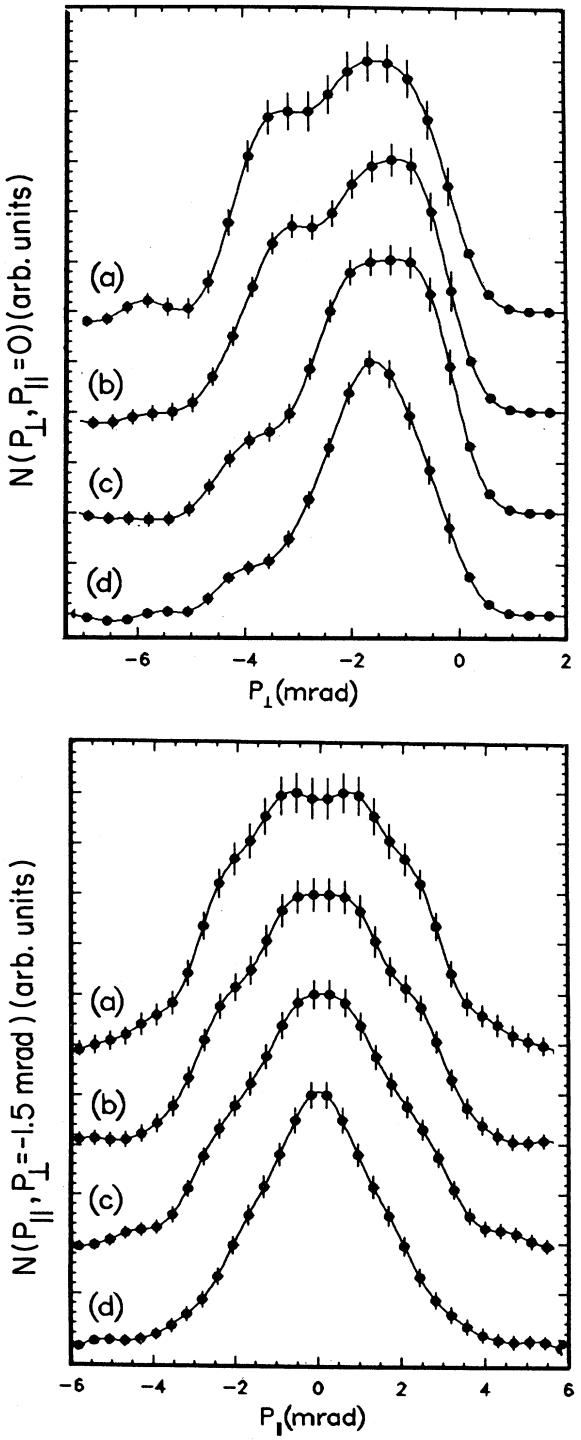

FIG. 16. Sections through $p_{\parallel}=0$ (top frame), and $p_{\perp}=-1.5$ mrad (lower frame) of the set of Ps spectra shown in Fig. 15, the alphabetical label corresponds to each frame in Fig. 15.

thus Φ_{Ps} is negative ($-2\sim-3$ eV) and the Ps emission from a surface into the vacuum is energetically favorable. Since the positron is thermalized prior to returning to the surface, by energy conservation the maximum-allowed Ps emission energy is $-\Phi_{Ps}$, and only electrons between the Fermi level E_F and $E_F+\Phi_{Ps}$ are the possible participants in the Ps formation and emission. The energy or momentum distribution of the emitted Ps atoms must be governed by the initial state of the surface and by the Ps formation mechanism.

The central issue of whether this electron pickup at a metal surface is an adiabatic or a sudden process was first explored by Mills *et al.*[15] by employing the TOF technique to measure the velocity distribution of the triplet Ps emitted from an Al(111) surface.[32] Their study showed that the Ps formation is a sudden process which leaves the solid in a one-hole excited state and hence allows for a simple interpretation via a single-particle picture. In its simplest form, the momentum density for Ps emission from a metal surface is

$$\rho_{Ps}(\mathbf{q}) \propto \sum_{l,\mathbf{k}} |M_{l,\mathbf{k}}|^2 n_l(\mathbf{k}) \delta\{E(\mathbf{q})+[E_F-E_l(\mathbf{k})]+\Phi_{Ps}\} , \tag{9}$$

where $\mathbf{q}$ is the Ps momentum, $\mathbf{k}$ is the crystal momentum, l is the energy band index, $n_l(\mathbf{k})$ is the occupation number, $M_{l,\mathbf{k}}$ is the transition matrix element, and the thermal momentum and energy of the positron have been neglected. Since the Ps is formed with electrons near the Fermi surface, it is plausible to assume a constant matrix element, apart from a δ function representing the translational symmetry along the surface. Thus to the first-order approximation,

$$\rho_{Ps}(\mathbf{q}) \propto \sum_{l,\mathbf{g},\mathbf{k}_\parallel} n_l(\mathbf{k}) \delta(\mathbf{q}_\parallel-\mathbf{k}_\parallel-\mathbf{g}) \times \delta\{E(\mathbf{q})+[E_F-E_l(\mathbf{k}_\parallel)]+\Phi_{Ps}\} , \tag{10}$$

where $\mathbf{g}$ is the surface reciprocal lattice vector. Since the Ps work function Φ_{Ps} is relatively small, only $\mathbf{g}=0$ can satisfy both δ functions. Equation (10) implies that the Ps formation must conserve both the energy and the momentum parallel to the surface, and that the momentum distribution is simply proportional to electron density of states near the Fermi surface.

For a free-electron gas, the two conservation laws are (in atomic units)

$$\mathbf{q}_\parallel=\mathbf{k}_\parallel , \tag{11}$$

$$\tfrac{1}{4}q^2=-\Phi_{Ps}-(E_F-\tfrac{1}{2}k^2) , \tag{12}$$

and the sum in Eq. (10) can be carried out to yield

$$\rho_{Ps}(\mathbf{q}) \propto q_\perp[q_\perp^2-q_\parallel^2-q_\parallel'^2+4(E_F+\Phi_{Ps})]^{-1/2} \quad \text{for } 0<|\mathbf{q}|<q_M , \tag{13}$$

where $q_M=\sqrt{-4\Phi_{Ps}}$, is the maximum Ps momentum. When $q_M<k_F$, which is often the case, we obtain from Eq. (1) the Ps ACAR spectrum for a free-electron gas:

$$N_{Ps}(q_\perp,q_\parallel) \propto \arcsin\left[\left[\frac{-4\Phi_{Ps}-q_\parallel^2-q_\perp^2}{4(E_F+\Phi_{Ps})-q_\parallel^2+q_\perp^2}\right]^{1/2}\right] . \tag{14}$$

A contour map of Eq. (14) is given in Ref. 1 for comparison with a measured Cu spectrum. For Al, $\Phi_{Ps}=-2.6$ eV, Eq. (14) gives a similarly isotropic contour map but with a characteristic semicircular cutoff at $q_M=\sim4.5$ mrad, which is in good agreement with our experimental spectra (Fig. 13). However, as will be shown below, the strong face dependence of the anisotropic structure present in our experimental spectra can be obtained only when more realistic projected energy-band structure for each of the Al surface is used instead of the free-electron gas.

C. Al surface electronic structures

To obtain the projected bulk-Al bands, we have used the bulk band structure of Al calculated using Harrison's Al pseudopotential and a plane-wave basis.[33] For each face we set up a mesh in the irreducible portion of the standard surface Brillouin zone (BZ) and then for each $\mathbf{k}_\parallel$-mesh point we vary k_z in the 3D BZ to generate the projected bands. Figure 17 shows the projections on the high-symmetry lines (see the inset) for each of these surfaces. The bottom of the bands are parabolic and substantial gaps appear below and above the Fermi level, especially in the (100) and the (110) projections. This nearly free-electron nature is primarily due to the trivalent atomic configuration of Al, the conduction bands being filled or half-filled with two s electrons and one p electron per atom. With the assistance of Fig. 18, the origin of these gaps can be easily tracked back to the gaps at the boundaries of the 3D BZ.[34] For instance, the gap around $\bar{\Gamma}$ (also from $\bar{\Gamma}$ to $\bar{X}$ and from $\bar{\Gamma}$ to $\bar{M}$) of the (100) face is associated with the gap at the zone boundary across X and perpendicular to ΓX, which is also responsible for the gap around the $\bar{X}$ point of the (110) face.

Several theoretical[35] and experimental[36] investigations have shown that localized surface states exist in these gaps. The true surface states appear close to the bottom of the gaps and follow a two-dimensional parabolic dispersion which extends into the resonant region. As an example we show in Fig. 19 the results of the angle-resolved photoemission experiment reported in Ref. 36(b). The shaded areas are the gaps shown in Fig. 17, the chain-dotted curves and the dashed curves are the surface states and resonant states, respectively. The solid curve will be discussed later. We omit the surface states existing inside the two narrow gaps of Al(111) which were demonstrated in Ref. 36(d).

In general, from the nearly free-electron nature of Al we would anticipate that projected gaps exist in the "off-high-symmetry" directions as well, and occupy some domains in the 2D BZ. In Fig. 20 we plot the projections (shaded) on the irreducible portion of the 2D BZ of the gap around $\bar{\Gamma}$ in the (100) face and the gap around $\bar{X}$ in the (110) face. For the (111) face we only project the gap

at $\frac{3}{4}$ of the way from $\bar{\Gamma}$ to $\bar{M}$ moving up to Fermi level. The projection within the whole zone can easily be mapped out by unfolding these portions throughout the zone. As suggested by these projected band gaps, surface states and surface resonant states have also been predicted[37] in all the gaps in addition to the high-symmetry lines, even though no experimental evidence has been reported explicitly.

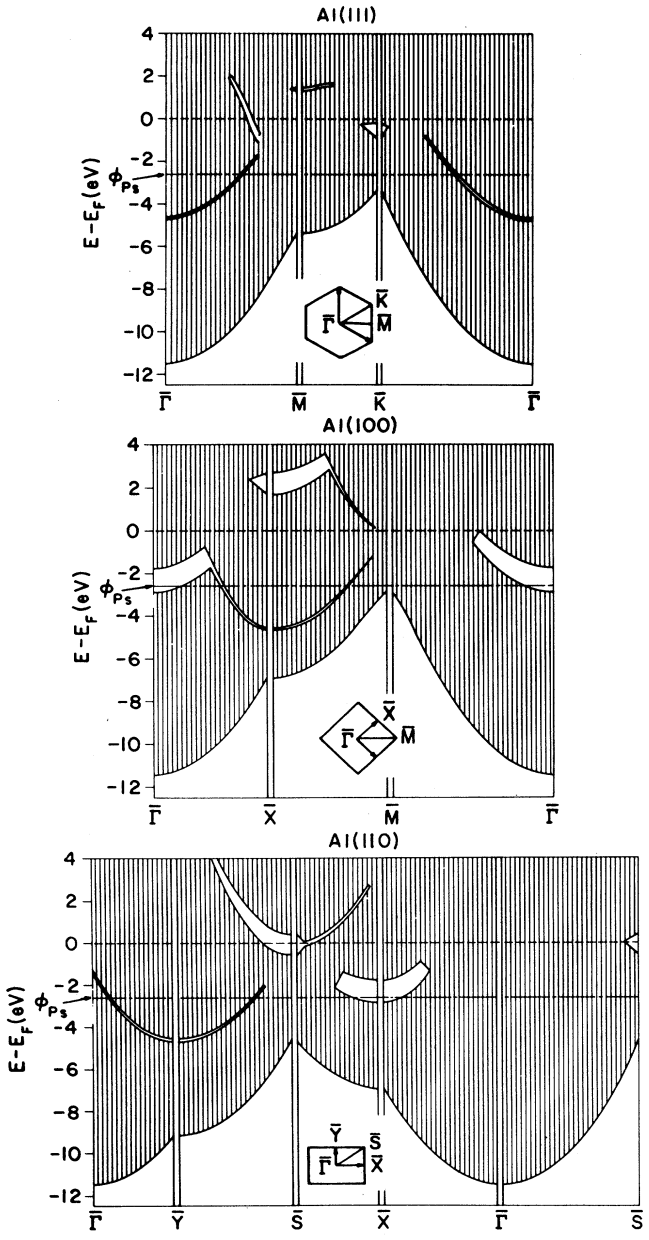

FIG. 17. Projected aluminum band structure along high-symmetry line of the surface Brillouin zone (BZ) shown in the inset. The bulk-Al band structure is calculated using Harrison pseudopotential and a plane-wave basis. The straight lines at −2.6 eV mark the positronium work function for Al.

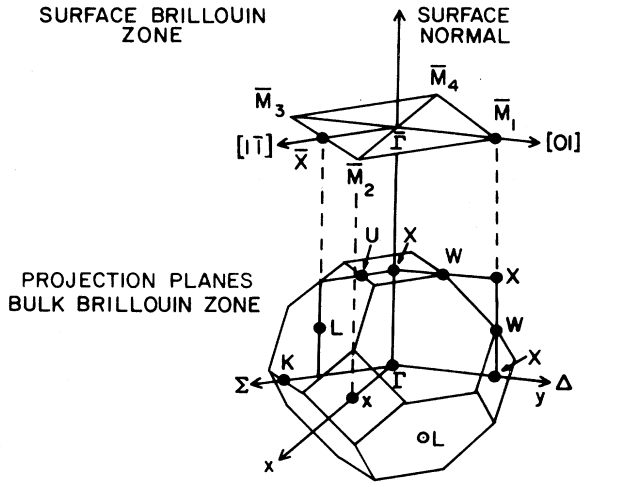

FIG. 18. The (100) projection of the 3D BZ of a fcc lattice onto a 2D BZ (Ref. 34).

D. Nearly free-electron approximation

The projected band structures of the three low index surfaces of Al shown in the preceding section have important consequences on the Ps momentum distributions as one would expect according to Eq. (10). In Fig. 17 the horizontal solid lines, which are 2.6 eV ($-\Phi_{Ps}$ for Al) below the Fermi level (dashed line), mark the lowest energy level for Ps formation. The presence of large gaps above this level already suggests that the real Ps momentum distribution differs significantly from the pure free-electron prediction of Eqs. (13) and (14). More precisely, the parallel momentum must be conserved at the same time the energy is conserved. It follows from Eqs. (11) and (12) that the kinetic energy of an electron required for Ps formation is least when $q_\perp=0$, or Ps atoms are emitted parallel to the surface. This forms the boundary of the lowest states for Ps formation:

$$E(\mathbf{k}_\parallel)=E_F+\Phi_{Ps}+\tfrac{1}{4}|\mathbf{k}_\parallel|^2 , \tag{15}$$

which are plotted as solid curves in Fig. 19. Together with the Fermi level (dashed lines) they determine an accessible region for Ps formation. Clearly a large portion of the projected gap in the Al(100) surface is within this region. It is smaller for the (110) face and least for the (111) face. Our analysis is not yet complete without inspecting these effects throughout the whole 2D BZ. In Fig. 20 we see that within the circle of radius q_M, the maximum Ps momentum, the (100) BZ contains largest projected-gap area around the $\bar{\Gamma}$ point, and according to Fig. 19, ~90% of the gap is in the accessible region. Although the (110) face also contains a large area of the gaps, it centers around the $\bar{X}$ point and most of it is below the boundary of the lowest states. Again, the (111) face contains the least. This qualitative analysis provides us an explanation for the strong surface face dependence of the measured Ps momentum spectrum.

More quantitatively, we insert these gaps into the free electron Fermi sphere to form a more realistic electron

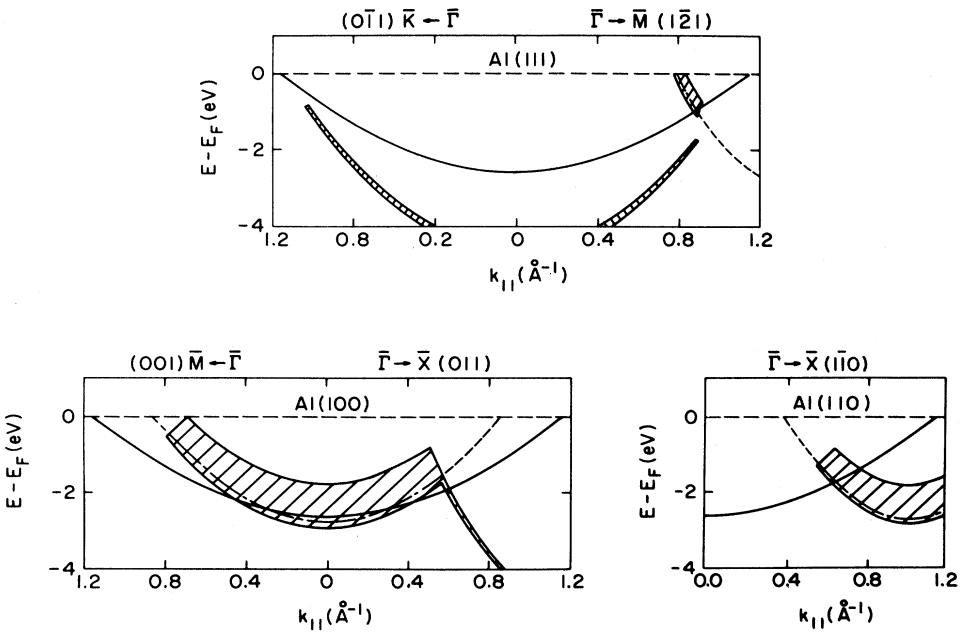

FIG. 19. Shaded areas are the projected Al band gaps reproduced from Fig. 17. The dot-chained and dashed curves are, respectively, the dispersions of the true surface state and surface-resonant state. Solid curves are the lowest occupied states that can form Ps atoms.

density function $n_l(\mathbf{k})$. The top and the bottom of the gaps (Fig. 19) can be represented by the parabolic dispersion:

$$E_g(\mathbf{k}_\parallel)=E_g+\frac{(\mathbf{k}_\parallel-\mathbf{k}_g')^2}{2m^*}\ , \tag{16}$$

where m^* is the effective mass. At the edge they are joined by a straight line. All the parameters, E_g, $\mathbf{k}_g'$, and m^* are obtained from fitting this parabolic curve to the projected band structures in the whole 2D BZ. They are listed in Table II. To simplify the computation the dashed curves in Fig. 20 are used as edges of the boundaries shown in solid curves.

Figure 21 shows the predicted Ps spectra for the three low index surface of Al. In order to make comparisons with the experimental spectra shown in Fig. 13, they have been convoluted with a two-dimensional Gaussian function having the same FWHM as our detector's resolution function (1 mrad×1 mrad). Both Al(111) and Al(110) spectra [21(a) and 21(c)] are similar to a free-electron prediction of Eq. (14). Close inspection shows that Al(110) spectrum 21(c) is slightly more forward at small $p_\perp$ compared with the Al(111) spectrum 21(a). This can be understood because the gap in the (110) face is near E_F (Fig. 19) and is in the large $|\mathbf{p}_\parallel|$ region. As might have been expected from the above discussion, the Al(100) spectrum 21(b) differs considerably from 21(a) and 21(c). It exhibits an anisotropic structure due to the large energy gap around $\bar{\Gamma}$. The predicted Ps ACAR spectrum for a 45° azimuthal rotation of the Al(100) surface is shown in Fig. 22(a). It is similar to Fig. 21(b) but the three lobes are slightly enhanced. To better visualize the anisotropy, Figs. 23(a) and 23(b) plots the perspective views of Figs. 20(a) and 20(b). These predictions are in good agreement with the experimental spectra (Figs. 13 and 14) for (i) an isotropic distribution is predicted for the Al(111) and Al(110) surfaces and the three lobes anisotropy for the Al(100) surface and (ii) azimuthal rotation by 45° of the Al(100) surface causes only small changes. Therefore, we are not precluded from concluding that the anisotropy in the Al(100) spectra stems from the shape of the projected energy gaps centered at $\bar{\Gamma}$ in the 2D BZ.

TABLE II. Fitted parameters for band-gap boundaries. $\omega\approx 1+\sin^2\phi$, where ϕ is the angle with respect to $\bar{X}\,\bar{\Gamma}$ and the origin is at $\bar{X}$. Parameters for Al(111) are averaged.

	E_g-E_F (eV)		$k_g(\pi/\bar{a})$		$m^*(m_e)$	
	Top	Bottom	Top	Bottom	Top	Bottom
Al(100)	−1.76	−2.89	0	0	1.02	1.00
Al(110)	−1.79	−2.86	1	1	1.02ω	1.00ω
Al(111)	−1.77	−2.88	$2\sqrt{3}$	$2/\sqrt{3}$	0.60	0.58

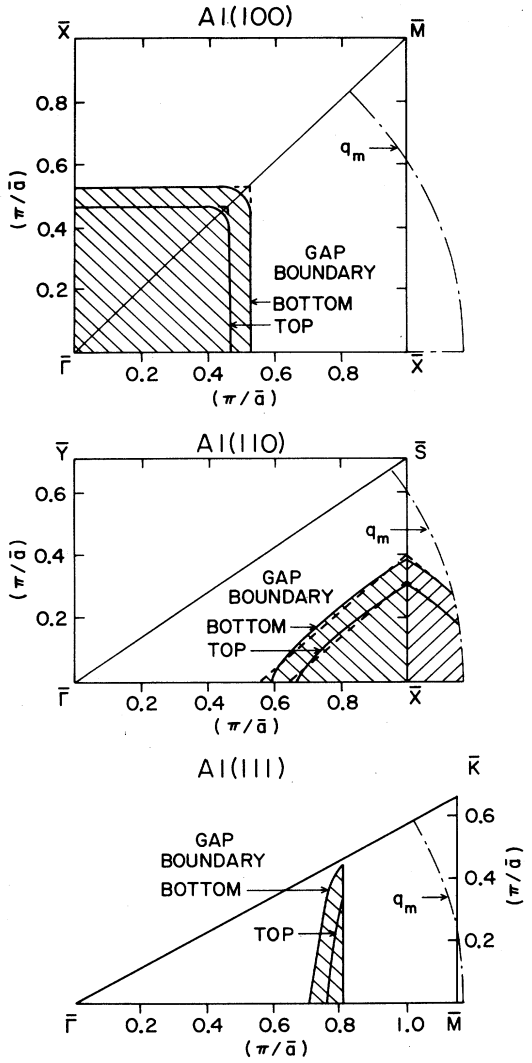

FIG. 20. Shaded areas are the projections of the gaps in the surface band structure. For the (111) face the gap is projected up to Fermi level, the lower narrow gaps and the gap at $\bar{K}$ are not projected. The dot-chained curves indicate the maximum-allowed Ps parallel momentum or electron parallel momentum in the extended zone scheme. $\bar{a}=a/\sqrt{2}$ for Al.

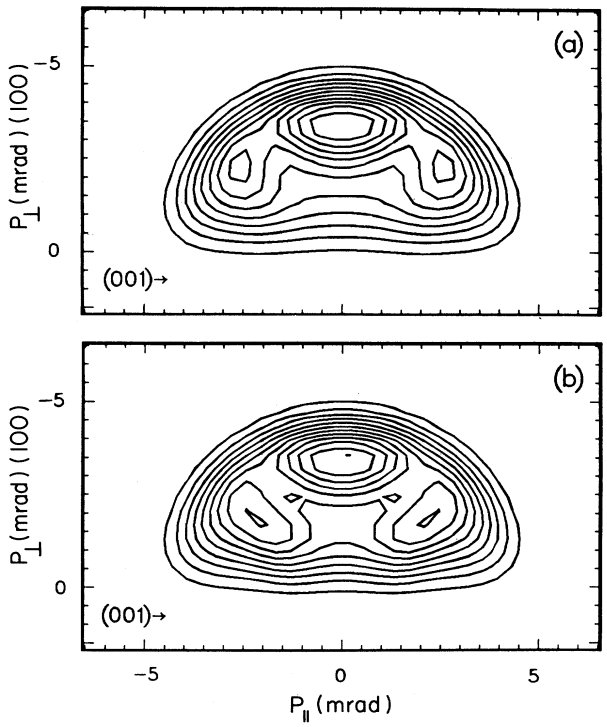

FIG. 22. Theoretical predictions of the Ps spectrum. (a) Nearly free-electron model for an Al(100) surface being rotated 45° azimuth with respect to Fig. 21(b), the projection is along $\bar{\Gamma}\bar{M}$. (b) Sum of the nearly free-electron prediction (a) with 20 vol % contribution from the surface-state electrons.

The theoretical prediction of the positions and relative shape of the lobes in the Al(100) Ps spectra depend on the width and the positions of the gaps in the surface band structure. A recent angle-resolved photoemission experiment[34] showed that the mapped width of the gap at X point (projected onto the $\bar{\Gamma}$ point) is about 0.5 eV wider than the theoretical prediction. These observations may need to be taken into account when a more precise quantitative prediction is desired. Since the Ps formation is believed to occur only at the surface, the role of the localized surface-state electrons need to be considered, though the total number of these electrons are much smaller than the regular bulklike electrons extended into the vacuum.

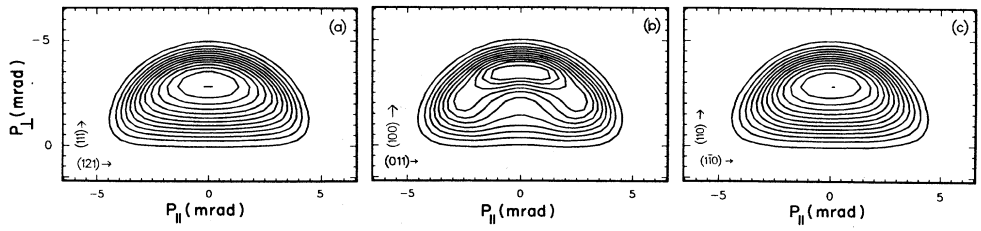

FIG. 21. Nearly free-electron-model predictions of the Ps spectrum for Al(111), Al(100), and Al(110) surfaces. They have been convoluted with a Gaussian detector resolution function for comparison with experimental spectra shown in Fig. 13.

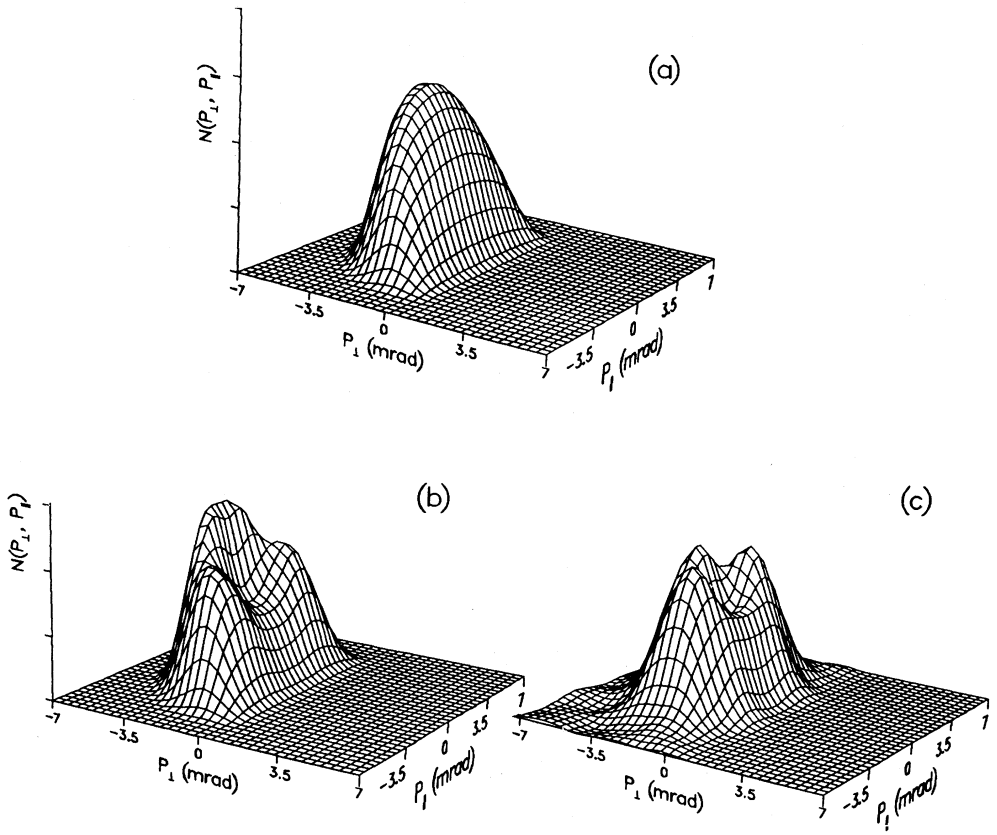

FIG. 23. (a) and (b) perspective representation of Figs. 21(a) and 21(b); (c) difference between the spectra for a clean-Al(100) surface [Fig. 14(a)] and 1 ML oxygen on the Al(100) surface [Fig. 14(b)].

To include this in our model we use the result of Ref. 36(b) (see Fig. 19) and assume a 0.1-eV bandwidth of these surface states and the same effective mass in all directions. In Fig. 22(b) we show as an example the effect of adding a 20 vol % surface-state-electron contribution into the nearly free-electron prediction of Fig. 22(a). The surface-state electrons cause the two side lobes to increase a little and shift towards each other. The agreement with the measured spectra [Fig. 14(a)] improved only slightly. However, the fraction of surface-state electrons added was somewhat arbitrary. Since these measured surface states are essentially located at the bottom of the projected band gaps (Fig. 19), the observed structures can be attributed mainly to the projected density of states. Another interesting observation can be made from the comparison of Ps formation with photoemission. In the "three-step" model of photoemission,[38] only those photoexcited electrons whose normal component of the kinetic energy is greater than the surface barrier are allowed to escape into the vacuum, which results in a cone emission. If we were to imagine the electron pick-up process as the electron being pulled over the potential barrier by the positron, then a similar restriction would lead to a 45° cone emission of Ps atoms regardless of the surfaces as long as the Φ_{Ps} is negative. This is clearly inconsistent with our experimental results shown in the previous section. In the case of Ps formation, the attractive Coulomb interaction between the positron and electrons produces a strong screening. Therefore the surface barrier does not affect the quasineutral Ps atoms in the same way as it does the photoelectrons.

Despite the reasonableness of the theoretical predictions, a discrepancy exists between the theoretical spectra and the measured spectra in the low-momentum region. All the experimental spectra (Fig. 13) exhibit dense contour lines around the origin indicating an enhanced low-momentum component of Ps emission, while the theoretical spectra are more peaked towards the maximum Ps momentum. This is shown most clearly in the $p_\parallel = 0$ sections in Fig. 24. The possible origins of the measured low-momentum component are (i) the oxygen contamination of the sample surface, (ii) momentum dependence of the transition matrix element, and (iii) some inelastic processes involved in the Ps formation.

E. Effect of oxygen contamination

We have shown in Figs. 15 and 16 that the Ps spectroscopy has a remarkable sensitivity to oxygen contamination on Al surfaces, and that the low-momentum component in the Ps spectrum grows as the oxygen contamination increases. To explore the possibility that the

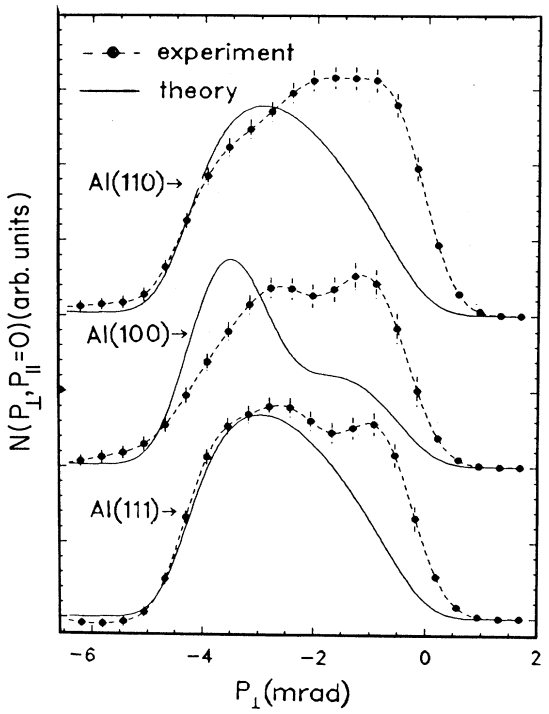

FIG. 24. $p_{\parallel}=0$ sections of the experimental (dashed) and theoretical (solid) Ps spectra (Fig. 21) for three low index surface of Al. The original 2D spectra are volume normalized.

difference between the theory and experiment is due to the oxygen contamination, we subtract from the clean-Al(100) run 40 vol% of the 150 L oxygen-exposed Al(100) surface run. The result is displayed in Fig. 23(c). It exhibits three lobes very close to those in Fig. 23(b) for the predicted Al(100) spectrum. A similar result is also obtained from subtracting Fig. 15(d) from Fig. 15(a). Furthermore, a higher intensity of the low-momentum component observed in the Al(110) spectrum [Fig. 13(c)] can be consistently attributed to the higher oxygen sticking probability on this surface.[23]

From the theoretical point of view, that oxygen contamination induces low-momentum Ps cannot be due to the change of the surface electronic structure alone. First, it was shown[31] that for chemisorbed oxygen on Al(111) and Al(100) surfaces, all the O_2 p electrons are lying below 5 eV from the Fermi level, and thus cannot participate in the Ps formation. Second, the presence of the oxygen atoms in or on the surfaces of Al leads to some charge transfer from Al atoms towards O atoms, and as a result Φ_- increases by 0.1 eV for Al(111) and decreases by 0.5–0.8 eV for Al(100) surface.[31] Because of the opposite potential-barrier contribution, an opposite change in Φ_+ is anticipated, hence Φ_{Ps} should remain unchanged and the direct Ps formation and emission should not be affected. Third, the chemisorbed oxygen on the Al(100) surface causes the surface states existing in the clean surface to shift towards the Fermi level and become resonant states.[31] These states could only give rise to a high-momentum component in the Ps emission.

Nieminen and Puska[16(b)] have shown theoretically that the ordered chemisorbed monolayers of oxygen on Al surfaces reduces the activation energy for the trapped positrons and hence make the image-potential-induced positron surface state unstable with respect to positronium emission even at room temperature. Although the emission of the thermal Ps from the surface-state positrons can account for the low momentum component in the Ps spectra, it seems difficult to explain why this oxygen-induced room-temperature activation only increases the total Ps fraction by 5%, while the total Ps thermal desorption from a clean-Al(100) surface at 600 K reaches 38% (see Sec. VII).

F. Transition matrix element

Our model assumes a constant matrix element. To include the possible momentum dependence of the transition matrix element in the Ps formation theory, a more complex calculation is required. Walker and Nieminen[39] have calculated the transition matrix element using a screened e^+-e^- interaction potential $U=e^{-\mu|\mathbf{r}^+-\mathbf{r}^-|}/|\mathbf{r}^+-\mathbf{r}^-|$. The electron wave function ψ_- and positron wave function ψ_+ for the initial state are obtained by assuming that electrons are confined by an infinite barrier a small distance ($\frac{3}{8}\pi k_F$) from the semi-infinite jellium edge, and that positrons see a step potential specified by $|\Phi_+|(\Phi_+<0)$. The overlap between the initial state and final state (free Ps) is restricted to a small surface region. Their result convoluted with a resolution function of 1.5 mrad FWHM is shown in Fig. 25(b). Comparing with our free-electron prediction, Fig. 25(a), their matrix element caused $\sim$0.5-mrad shift of the most probable Ps distribution toward lower $p_{\perp}$. However, this

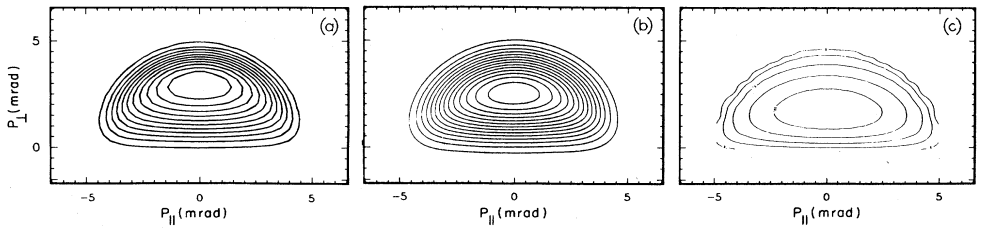

FIG. 25. The Ps spectrum from the theoretical prediction of (a) a free-electron model, (b) Walker and Nieminen (Ref. 39), and (c) Shindo and Ishii (Ref. 40).

does not remove the discrepancy in the low-momentum region exhibited in Fig. 24, and in the high-momentum region it worsens the agreement. It should be mentioned that their treatment was in first-order time-independent perturbation, and it ignored the possibility of electron-hole pair creation or the scattering of Ps once it is formed.

Ishii and Shindo have extended the ion neutralization theory to describe the Ps formation at metal surfaces.[40,41] The motivation of using this resonant charge-exchange model for the Ps formation came from the fact that the binding energy of the Ps state lies within the energy bands of a metal surface. The model includes in the Fermi's golden-rule formula higher-order terms describing both electrons hopping from the surface to the positron (Ps formation) and vice versa (Ps dissociation), an exponentially decaying dynamical factor to account for the decreasing transition magnitude with increasing distance between the Ps atom and the surface, and a quantum-mechanical description of the center-of-mass motion of the Ps because of its light mass. The dissociation term is essential in order to avoid the divergence at large angle of emission, which one encounters in the first-order Born approximation ($\propto 1/v_z$). It is shown that the transition matrix element is essentially constant, and the dynamical interaction enhances the small-momentum emission but smears the electron density of states near a metal surface. A prediction of the 2D ACAR spectrum for an Al surface from this theory[40] is shown in Fig. 25(c). The over enhancement of the low-$p_\perp$ component (or large angle emission) was attributed to the wide-band approximation which allows electrons to return to unrealistically wide unoccupied bands of the surface. Ishii and Shindo have also shown[40] that the energy and angular dependence of the Ps emission spectrum is sensitive to some testing band structures. Work using a more realistic Al electronic band structure is underway.

VII. THERMALLY ACTIVATED POSITRONIUM

In this section we give a quantitative analysis of the results presented in Sec. III B. There it was shown [Figs. 5(b) and 6] that when an Al(100) surface is heated to 600 K, a sharp narrow peak emerges near zero momentum on the negative $p_\perp$ side of the ACAR spectrum, which is accompanied by a large reduction of the positron surface-state annihilation component. This is the most direct evidence for the established picture that positrons captured in the surface states are thermally desorbed as Ps atoms. Note that the thermal peak in Fig. 5(b) has a width comparable with the detector resolution (~ 1 mrad) and its center appears almost at the origin. If the thermally desorbed Ps energy is on the order of $K_B T$, the width of the peak should be dominated by the apparatus resolution (~ 1 mrad). In fact, it is for this very reason our inversion-subtraction data-separation technique failed to decompose the thermal Ps spectra accurately.

To investigate further the projected thermal Ps momentum distribution we assume that at this elevated sample temperature the bulk, surface state, and directly formed Ps annihilation spectra do not change substantially from their room-temperature spectra. Hence the latter, when properly normalized, can be used to remove approximately their corresponding hot components from the high-temperature measurement to obtain the thermal Ps distribution. The contribution from each component can be estimated in a self-consistent manner. The yield of the thermal desorbed Ps should be equal to the reduced fraction of positrons captured in the surface states, assuming the temperature effect on the surface branching ratios is of higher order. The normalization factors are adjusted so that the intensity of the difference spectrum just approaches negative values which are, of course, unphysical. This approximation is reasonable since the thermal momentum is much smaller than the Fermi momentum, and Φ_-, Φ_+, and $\Phi_{\rm Ps}$ do not change appreciably compared with the most probable energy (~ 1 eV) of the directly emitted Ps. However, at 600 K about 10% of the implanted positrons are trapped and annihilate in the thermally activated vacancies,[8] producing a spectrum with a width lying between the extended bulk state and external surface-state spectrum.[5,25] Fortunately this is a small fraction, and we will not attempt to make any correction here.

Figure 26 illustrates this method with the $p_\parallel = 0$ sections. The normalization factors indicated in the figures are the volume percentage with respect to the total measurement. In Fig. 26(a) the symmetrical component (dashed curve) consists of 25 vol % surface state and 43 vol % bulk spectra obtained at room temperature. This gives a good approximation, and the small deviation is attributable to a small thermal broadening or more likely to the trapping of positrons in vacancies. The difference curve (dots) is the extracted total Ps spectrum which clearly shows a cutoff at ~ -4.5 mrad as expected. In Fig. 26(b), 40 vol % of the room-temperature Ps spectrum coincides well in the large-momentum region with the extracted total Ps spectrum, hence the difference (dots) is taken as the thermal Ps distribution. From the normalization factors we estimate that $f_{\rm bulk} = 22\%$, $f_{\rm SS} = 13\%$, and $f_{\rm Ps} = 65\%$ of which 38% are thermal Ps. Thus the bulk fraction remains almost the same as the room-temperature fraction, the direct formation of Ps is reduced by $\sim 5\%$ and $\sim 84\%$ surface-state positrons are thermally desorbed as Ps.

The activation energy for a positron bound in a surface potential well with a binding energy E_b to be librated as a Ps atom is

$$E_a = E_b + \Phi_- - \tfrac{1}{2} R_y \ , \tag{17}$$

which is typically a few hundreds meV. Chu *et al.*[42] have described the Ps thermal activation process in terms of thermodynamics similar to those leading to the Richardson-Dushman equation for ordinary thermionic electron emission. They derived the Ps thermal emission rate

$$z = \frac{4 K_B T}{h} \exp(-E_a / K_B T)(1 - \langle r \rangle) \ , \tag{18}$$

where K_B and h are, respectively, the Boltzmann and

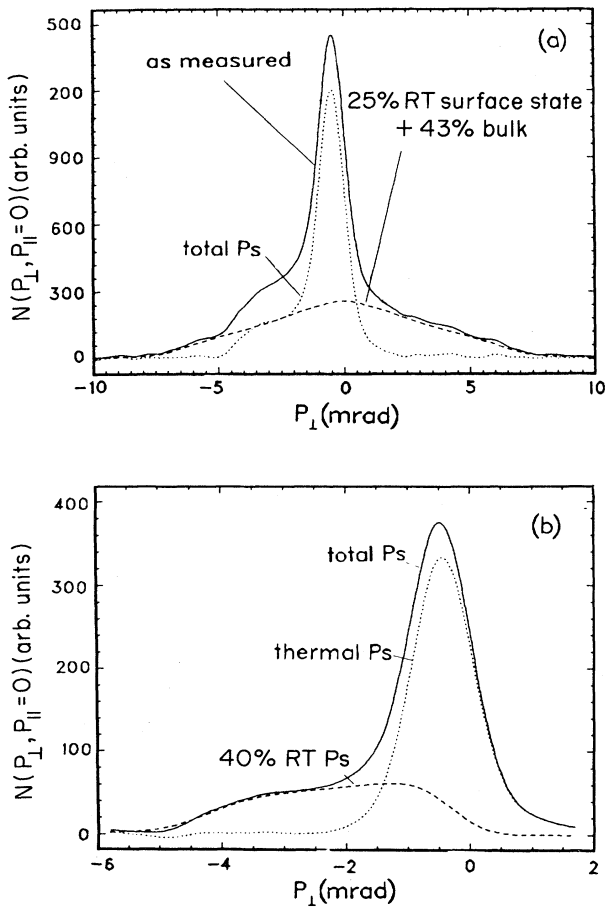

FIG. 26. (a) $p_\parallel=0$ sections of the total measurement (solid curve) for an Al(100) surface at 600 K and 1.5-keV incident energy, a composed symmetrical spectrum (dashed) containing 25 vol % room-temperature surface-state spectrum and 40 vol % room-temperature bulk spectrum, and their difference (dotted). (b) $p_\parallel=0$ sections of the extracted total Ps spectrum [see (a)], 40 vol % room-temperature Ps spectrum, and the deduced thermal Ps spectrum.

Planck's constants, and $\langle r \rangle$ is the average of the Ps surface reflection coefficient $r(q_\perp)$ over the distribution of the Ps thermal velocities. The probability of converting a positron in the surface state to a free thermal Ps is $z/(z+\gamma)$, where γ is the positron surface-state annihilation rate. From the analysis of their TOF experiment for the normal emission thermal Ps from an Al(111) surface, Mills and Pfeiffer[24(c)] obtained $E_a=0.344$ eV, $(1-\langle r \rangle)=0.21$, and T to be within 10% of the measured temperature. Their data also showed that $r(q_\perp)$ is essentially constant. Using these fitted parameters for the Al(111) surface and $\gamma=1.72$ nsec^{-1} for an Al(110) surface reported by Lynn *et al.*,[30] we estimate that at 600 K 62% of the surface-state positron are thermally activated. This is about 20% lower than our estimate for an Al(100) surface. The earlier Ps fraction study by Mills[24(a)] did not include the linear temperature term in Eq. (18), there they obtained for an Al(100) surface $E_a=0.64$ eV, and $(1-\langle r \rangle)z_0/\gamma=3.5\times10^6$. This leads to $z/(z+\gamma)=93\%$, about 10% higher than our present estimate.

The statistical distribution of the thermal Ps momentum

$$\rho^T_{Ps}(\mathbf{q})=\exp(-q^2/4mK_BT)[1-r(q_\perp)]\cos\theta\ , \qquad (19)$$

where the Knudsen's cosine law has been included and the reflection coefficient is in general a function of the normal momentum. The TOF measurement of Mills and Pfeiffer[24(c)] showed that it agrees well with the data obtained in a normal-emission geometry. Our ACAR data provide the first comparison between experiment and the angular-dependent theoretical distribution of Eq. (19). Figure 27 shows the projected spectrum of Eq. (19) against the extracted thermal Ps spectrum (dots). We note that the agreement is quite good. A few observations have to be made. (i) When the sample size effect is not included in the resolution function, the agreement between the theory and data is much poorer in the parallel sections, this is due to the very narrow distribution of the thermal Ps. (ii) A preference for a constant Ps reflection coefficient $r(q_\perp)$ is found in our fitting, consistent with the TOF study of Mills and Pfeiffer.[24(c)] Pendry[43] has predicted $1-r(q_\perp)=q_\perp$ which results in a distribution too far forward compared with the measurement. (iii) The convoluted spectrum is less sensitive to the variation of temperature, no appreciable difference can be observed within ±50 K. At present condition, the width of the detector resolution dominates the spectrum width. Clearly a higher precision study awaits for better detector resolution.

VIII. SUMMARY AND CONCLUSIONS

Using a high-intensity, low-energy positron beam and an UHV surface chamber constructed at Brookhaven National Laboratory, we have successfully applied the well-established 2D ACAR technique to study the interactions of positrons with three low index surfaces of aluminum. Effects of the adsorption of oxygen on aluminum surfaces have also been explored. Our measurements confirmed three important processes: spontaneous Ps formation and emission, positrons bound in a surface state, and thermally desorbed as Ps atoms. Based on the inversion symmetry of the bulk and surface-state momentum density functions, an "inversion-subtraction" data decomposition technique employing the van Cittert's deconvolution algorithm has been developed to separate the Ps component and the surface-state component from the directly measured spectrum.

Our measured annihilating spectra for the positron surface state are considerably narrower than in the extended bulk state. This difference is a result of the inhomogeneous electron density at the surface and the localization of positrons at the surface. However, we obtained an essentially isotropic surface-state annihilation spectrum for all the studied surfaces of Al. This is inconsistent with either the image-potential-induced positron surface-state model, or the physisorbed Ps surface-state model; both

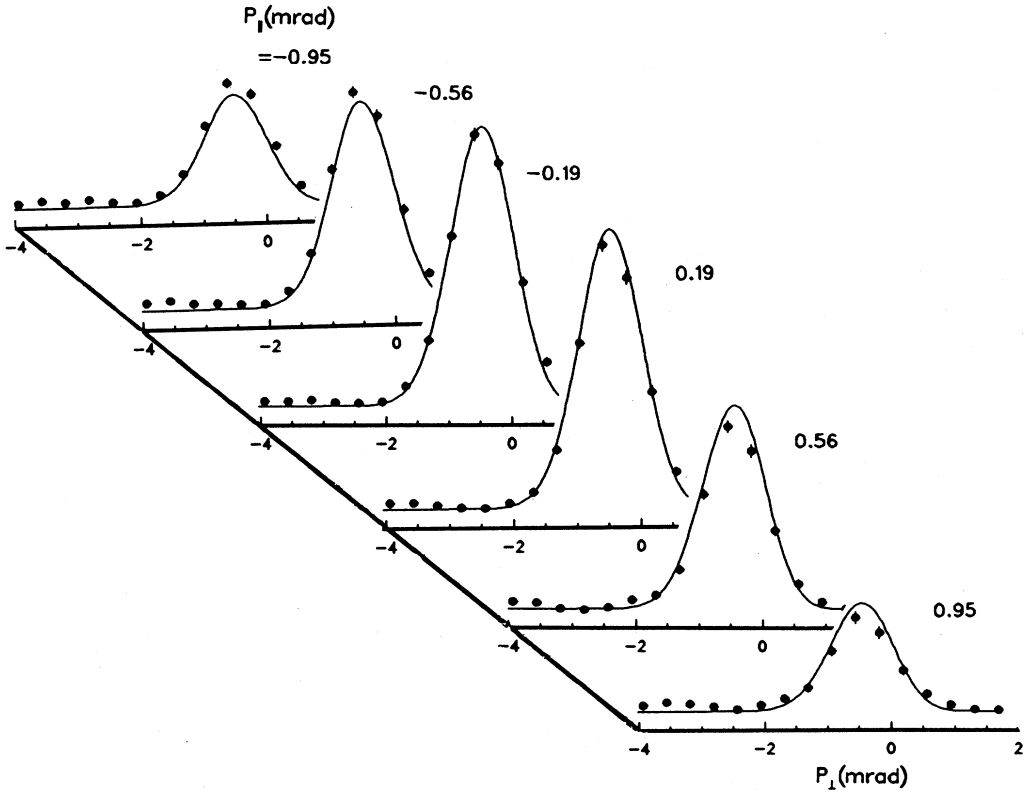

FIG. 27. The statistical distribution of the thermal Ps (solid lines) vs the extracted data (dots) at 600 K. They are peak normalized. A constant reflection coefficient is used in the model.

predicting large anisotropies due to the localization perpendicular to the surface and delocalization parallel to the surface of the bound positron or Ps. Although the emission of a surface plasmon may lead to an isotropic distribution of the bound Ps surface-state annihilation, the theoretical width is too narrow in comparison with our measurement. The lack of an anisotropy in the experimental data suggests a lateral localization of the positron resulting from trapping by surface defects or impurities. This conjecture needs to be verified in further studies.

We have demonstrated that the Ps momentum distribution reflects the electron density of states near the surface. In particular, it reveals the projected band gaps in Al surfaces with strong face-dependent, directional anisotropies. These results imply that Ps 2D ACAR spectrum might offer us a new angle-resolved surface spectroscopy. Since the final state of the Ps formation is well defined (e^+-e^- bound state), this technique has an advantage over the angle-resolved photoemission which often assumes free electron final states in order to map out the band dispersion of the initial states. Clearly, the feasibility of the angle-resolved Ps spectroscopy depends crucially on whether or not it is significantly contaminated by some complicated inelastic effects or by higher-order transitions. We have seen that the measured Ps spectra for Al contains an enhanced low-momentum component which cannot be explained by the simple nearly free-electron model. Future measurements with improved experimental conditions are required to determine whether this enhancement is due to a small amount of oxygen contamination or is intrinsic to a Ps formation mechanism.

The Ps momentum spectroscopy is limited by energy conservation to a narrow energy band of ~ 2 eV ($-\Phi_{Ps}$) below the Fermi level for most of the metals (except alkali metals) and semiconductors. This suggests that to further understand the Ps formation mechanism measurement on *d*-band metals is of great importance, because the density of states (DOS) near the Fermi level are considerably increased due to the *d* electrons. A preliminary measurement[11] on Ni indeed showed an enhanced Ps momentum intensity near the cutoff compared with the Ps spectrum of Al. However, the structure in the DOS for the majority and minority states cannot be identified and are most probably smeared out by the limited detector resolution. These experiments need to be repeated when higher resolution detectors are available. In addition, the induced localized surface-state electron wave functions of Ni are predicted to be quite distinct from the bulk conduction electron wave functions at the surface[37] and might play an important role in Ps formation, as contrasted with the electron surface states in Al. Energy conservation also restricts the formation and

emission of the umklapp Ps atoms [Eq. (7)] for most of the unreconstructed surfaces. We note, however, that ϕ_{Ps} is close to -5 eV for a W surface (~ -4 eV for Cr)[7] and also *W* surfaces reconstruct. Thus it could be a good candidate for demonstrating the umklapp Ps formation effect.

In our present experiment, a small fraction of the reemitted slow positrons eventually return to the biased sample surface and take part in either the surface-state annihilation or the Ps formation. It is important to know whether or not these returning positrons form Ps via some different mechanism. For example, they may form Ps while approaching the surface from a vacuum, which then would be connected to the Ps formation by glancing angle scattering or back scattering.[44] This effect should be studied with materials of large slow positron emission yield such as Ni, W, Cu, etc.

In this paper we also present the first two-dimensional momentum distributions of the thermally desorbed Ps. The ACAR spectra demonstrate *directly* the fact that these thermal Ps atoms originate indeed from the positrons trapped in a surface state at lower temperature (<300 K). These thermal Ps momentum distributions are shown to agree well with the theoretical description of the thermodynamical emission process. However the sensitivity of our measurement to the temperature is clearly limited by the present detector resolution. Although our analysis indicates that a constant Ps reflection coefficient produces better agreement with experimental data, we do not have systematic measurements to verify the temperature dependence of the reflection coefficient. The establishment of this parameter would provide us with some insight into the detailed desorption mechanism. High precision ACAR study on this subject requires detectors with a resolution better than 0.5 mrad FWHM.

As has been shown throughout this paper, our data-separation technique is accurate except for the high-temperature surface data which is dominated by the large fraction of thermal Ps. Theoretical predictions[7] have indicated that for alkali metals $\Phi_{Ps}>0$, hence spontaneous Ps emission is forbidden. For these surfaces the asymmetric Ps component, therefore, should not appear in the measurement, and it will be interesting to observe the obvious inversion symmetry of these spectra.

It is clear that many of our uncertainties at present stage can be removed once a more intense slow positron beam and better resolution detectors become available. Owing to the recent discovery of the new solid-Ne moderator,[45] it is anticipated that the slow positron beam intensity can be increased (in the near future) by at least one order of magnitude. Efforts to reach this goal are currently under way.

ACKNOWLEDGMENTS

The authors wish to thank J. Hurst, T. Homquist, R. Lee, J. Ruthford, S. Z. Tang, M. Weber, and J. Zahradka for their technical assistance. This work was supported in part by the National Science Foundation (Grant No. DMR-8315691), a grant from The City University of New York PSC-CUNY Research Award Program, and the U.S. Dept. of Energy Division of Material Science (Contract No. DE-AC02-76CH00016).

APPENDIX: DATA ANALYSIS

1. Analysis procedures

To decompose a surface ACAR spectrum the following steps are taken sequentially: (1) Determine the position of $\mathbf{p}_{\parallel}=0$ and center the spectrum; (2) symmetrize the spectrum (when allowed); (3) deconvolute the spectrum; (4) perform the inversion subtraction; (5) convolute the separated spectra; (6) remove the bulk component (when necessary).

2. van Cittert's method

The van Cittert's iteration procedure for deconvolution can be expressed by

$$\Delta_i = N_0 - \int N_{i-1}(\mathbf{p}'_{\parallel}) R(\mathbf{p}_{\parallel}-\mathbf{p}'_{\parallel}) d\mathbf{p}'_{\parallel} , \tag{A1}$$

$$N_i = N_{i-1} + \Delta_i , \tag{A2}$$

where $R(\mathbf{p}_{\parallel}-\mathbf{p}'_{\parallel})$ is the detector resolution function, Δ_i and N_i are the ith order correction and solution, respectively. Note that after sufficient number of iterations the correction of Eq. (A1) contains essentially the noise component of the data. Thus

$$\int N_n(\mathbf{p}_{\parallel}) R(\mathbf{p}_{\parallel}-\mathbf{p}'_{\parallel}) d\mathbf{p}'_{\parallel} = N_0 - \Delta_{n+1} \tag{A3}$$

implys that convolution of the nth-order solution is equivalent to removing the noise from the original data, i.e., smoothing. Thus our separated spectra should have little distortion away from the narrow strip near $\mathbf{p}_{\perp}=0$.

3. Ps and bulk fractions

Define

$$V = \int N(p_{\perp}, p_{\parallel}) dp_{\parallel} dp_{\perp} , \tag{A4}$$

$$\eta = \frac{V_{Ps}}{V_{tot}} , \tag{A5}$$

which is the measured para-Ps fraction. In statistical average, $\frac{1}{4}$ of the ground-state Ps atoms are formed in the singlet state and $\frac{3}{4}$ are in the triplet state. Thus the total Ps fraction can be derived from

$$F_{Ps} = \frac{4\eta}{1+3\eta} . \tag{A6}$$

The residual bulk fraction in the total measurement is

$$\frac{V_{bulk}}{V_{tot}} = F_{bulk}(1+3\eta) , \tag{A7}$$

or

$$\frac{V_{bulk}}{V_{tot}-V_{Ps}} = F_{bulk}\frac{1+3\eta}{1-\eta} . \tag{A8}$$

F_{bulk} is the fraction of incident positrons which annihilate in the bulk. It can be calculated from the solution of the positron diffusion equation (see, for example, Ref. 5). Equations (A6)–(A8) are valid only if there is no slow positron emission. This condition can easily be guaranteed by applying a retarding field to repel any of the emitted positrons.

*Current address: Department of Physics, Harvard University, Cambridge, MA 02138.

[1]R. H. Howell, P. Meyer, I. J. Rosenberg, and M. J. Fluss, Phys. Rev. Lett. **54**, 1698 (1985).

[2]K. G. Lynn, A. P. Mills, Jr., R. N. West, S. Berko, K. F. Canter, and L. O. Roellig, Phys. Rev. Lett. **54**, 1702 (1985).

[3]K. G. Lynn, A. P. Mills, Jr., L. O. Roellig, and M. Weber, in *Electronic and Atomic Collisions,* edited by D. C. Lorentz, W. E. Meyerhof, and J. R. Peterson (North-Holland, New York, 1986), p. 227; K. G. Lynn, M. Weber, L. O. Roellig, A. P. Mills, Jr., and A. R. Moodenbaugh, in *Atomic Physics with Positrons,* edited by J. W. Hamberston and E. A. G. Armour (Plenum, New York, 1987), p. 161.

[4]D. M. Chen, S. Berko, K. F. Canter, K. G. Lynn, A. P. Mills, Jr., L. O. Roellig, P. Sferlazzo, M. Weinert, and R. N. West, Phys. Rev. Lett. **58**, 921 (1987).

[5]D. M. Chen, Ph.D. thesis, City University of New York, 1987.

[6]D. M. Chen, S. Berko, K. F. Canter, K. G. Lynn, A. P. Mills, Jr., L. O. Roellig, and R. N. West (unpublished).

[7]A. P. Mills, Jr., in *Positron Solid State Physics,* edited by W. Brant and A. Dupasquier (North-Holland, New York, 1983), p. 432, and references therein.

[8]K. G. Lynn, in Ref. 7, p. 609.

[9]S. Berko, in Ref. 7, p. 64, and references therein.

[10]R. N. West, Adv. Phys. **22**, 263 (1973).

[11]P. Sferlazzo, S. Berko, K. F. Canter, D. M. Chen, K. G. Lynn, A. P. Mills, Jr., L. O. Roellig, A. Viescas, and R. N. West, Bull. Am. Phys. Soc. **32**, 899 (1987).

[12]P. Sferlazzo, S. Berko, K. F. Canter, K. G. Lynn, A. P. Mills, Jr., L. O. Roellig, A. Viescas, and R. N. West, Phys. Rev. Lett. **60**, 538 (1988).

[13]R. H. Howell, I. J. Rosenberg, P. Meyer, and M. J. Fluss, Phys. Rev. B **35**, 4555 (1987).

[14]H. Kanazawa, Y. H. Ohtsuki, and S. Yanagawa, Phys. Rev. **138**, A1155 (1965); A. Held and S. Kahana, Can. J. Phys. **42**, 1908 (1964).

[15]A. P. Mills, Jr., L. Pfeiffer, and P. M. Platzman, Phys. Rev. Lett. **51**, 1085 (1983).

[16](a) C. H. Hodges and M. J. Stott, Solid State Commun. **12**, 1153 (1973); (b) R. Nieminen and M. Mannien, *ibid.* **15**, 403 (1974); (c) R. M. Nieminen and M. J. Puska, Phys. Rev. Lett. **50**, 281 (1983); (d) **53**, 1298 (1984).

[17](a) A. P. Brown, A. B. Walker, and R. N. West, J. Phys. F **17**, 2491 (1987); (b) A. P. Brown, Kjeld O. Jensen, and A. B. Walker, *ibid.* **18**, L141 (1988).

[18]J. Garner and R. Benedek, J. Phys. F **16**, L165 (1986).

[19]Yongmin Lou, Binglin Gu, Jialin Zhu, Chang Lee, and Jia Jiong Xiong (unpublished).

[20]P. M. Platzman and N. Tzoar, Phys. Rev. B **33**, 5900 (1986).

[21]L. O. Roellig, M. Weber, S. Berko, B. L. Brown, K. F. Canter, K. G. Lynn, A. P. Mills, Jr., S. Tang, and A. Viescas, in *Atomic Physics with Positrons,* edited by J. W. Humberston and E. A. G. Armour (Plenum, New York, 1987), p. 233.

[22]R. N. West, J. Mayer, and P. A. Walters, J. Phys. E **14**, 478 (1981).

[23]P. O. Gartland, Surf. Sci. **62**, 183 (1977); C. W. B. Martinson and S. A. Flodstrom, *ibid.* **80**, 306 (1979).

[24](a) A. P. Mills, Jr., Solid State Commun. **31**, 623 (1979); (b) A. P. Mills, Jr. and L. Pfeiffer, Phys. Rev. Lett. **43**, 1961 (1979); (c) Phys. Rev. B **32**, 53 (1985).

[25]M. J. Fluss, S. Berko, B. Chakraboty, K. Hoffman, P. Lippel, and R. W. Siegel, in *Positron Annihilation,* edited by P. G. Colman, S. C. Sherma, and L. M. Diana (North-Holland, New York, 1982), p. 454; A. Alam, J. H. Kaiser, P. A. Walters, R. L. Waspe, and R. N. West, *ibid.*, p. 331.

[26]In principle, a precise Ps component can be obtained from quenching the $m=0$ triplet state into the singlet state by a strong magnetic field; see A. P. Mills, Jr., J. Chem. Phys. **62**, 2646 (1974), and references therein.

[27]G. K. Wertheim, Rev. Sci. Instrum. **46**, 1414 (1975), and references therein.

[28]A long-slit ACAR spectrum is the one-dimensional projection of the momentum density function, which can be generated from the 2D ACAR spectrum by the following integrations: $N(p_\perp)=\int N(p_\perp,p_\parallel)dp_\parallel$, $N(p_\parallel)=\int N(p_\perp,p_\parallel)dp_\perp$.

[29]A. Dupasquier, in Ref. 7, p. 510.

[30]K. G. Lynn, W. E. Frieze, and P. J. Schultz, Phys. Rev. Lett. **52**, 1137 (1984).

[31]H. Krakauer, M. Posternak, A. J. Freeman, and D. D. Koellig, Phys. Rev. B **23**, 3859 (1981); Ding-Sheng Wang, A. J. Freeman, and H. Krakauer, *ibid.* **24**, 3092 (1981); **24**, 3104 (1981); **24**, 3614 (1981).

[32]The ground-state Ps is formed either in a singlet state ($s=0$, para-Ps) or in a triplet state ($s=1$, ortho-Ps). The statistically averaged ratio of the para-Ps yield to the ortho-Ps yield is 1 to 3. In contrast to the short para-Ps lifetime (125 ps), an ortho-Ps has a relatively long lifetime (145 ns) and can travel a distance on the order of 10 cm prior to annihilating into three photons. Thus the ortho-Ps is suitable for the time-of-flight measurement.

[33]W. A. Harrison, *Electronic Structure and Properties of Solids* (Freeman, San Francisco, 1980).

[34]Harry J. Levinson, F. Greuter, and E. W. Plummer, Phys. Rev. B **27**, 727 (1983).

[35](a) D. S. Boudreaux, Surf. Sci. **28**, 344 (1971); (b) E. B. Carathers, L. Kleinman, and G. P. Alldredge, Phys. Rev. B **8**, 4570 (1973); **9**, 3325 (1974); **9**, 3330 (1974); (c) J. R. Chelikowsky, M. Schulter, S. G. Lowis, and M. L. Cohen, Solid State Commun. **17**, 1103 (1975); (d) H. Krakauer, M. Posternak, and A. J. Freeman, Phys. Rev. Lett. **41**, 1072 (1978); Ding-Sheng Wang, A. J. Freeman, H. Krakauer, and M. Posternak, Phys. Rev. B **23**, 1685 (1981); (e) M. Seel, Phys. Rev. B **28**, 778 (1983).

[36](a) P. O. Gartland and B. J. Slagsvold, Solid State Commun. **25**, 489 (1978); (b) G. V. Hansson and Flodstrom, Phys. Rev. B **18**, 1562 (1978); (c) Peter Hofmann and Kyozaburo Kambe, *ibid.* **30**, 3028 (1984); (d) S. D. Kevan, N. G. Stroffel, and N. V. Smith, *ibid.* **31**, 1788 (1985).

[37]M. Weinert (unpublished data).

[38]*Photoemission I&II,* edited by M. Cardona and L. Ley (Springer-Verlag, New York, 1978).

[39]A. B. Walker and Nieminen, J. Phys. F **16**, L295 (1986).

[40]S. Shindo and A. Ishii, Phys. Rev. B **35**, 8360 (1987); **36**, 709 (1987); and unpublished.

[41]Akira Isii, Surf. Sci. **147**, 277 (1984); **147**, 295 (1984); **163**, 498 (1985); A. Ishii, Phys. Rev. B **35**, 6521 (1987).

[42]S. Chu, A. P. Mills, Jr., and C. A. Murray, Phys. Rev. B **23**, 2060 (1981).

[43]J. B. Pendry, in Ref. 7, p. 408.

[44]R. H. Howell, I. J. Rosenberg, and M. J. Fluss, Phys. Rev. B **34**, 3069 (1986); D. W. Gidley, W. E. Frieze, R. Mayer, and K. G. Lynn, Phys. Rev. Lett. **58**, 595 (1987).

[45]A. P. Mills and E. M. Gullikson, Appl. Phys. Lett. **49**, 1121 (1986).